System Identification and Control of an Arleigh Burke Class Destroyer Using an Extended Kalman Filter

by

Michael Eric Taylor
B.S., Civil Engineering
University of South Carolina, 1993

Submitted to the Departments of Ocean Engineering and Mechanical Engineering
in partial fulfillment of the requirements for the degrees of

Naval Engineer

and

Master of Science in Mechanical Engineering

at the

MASSACHUSETTS INSTITUTE OF TECHNOLOGY

June 2000

Author .....
Departments of Ocean Engineering and Mechanical Engineering
May 15, 2000

Certified by .....
Michael S. Triantafyllou
Professor of Hydrodynamics and Ocean Engineering
Thesis Supervisor

Read by .....
Derek Rowell
Professor of Mechanical Engineering
Thesis Reader

Accepted by .....
Nicholas M. Patrikalakis
Kawasaki Professor of Engineering
Chairman, Departmental Committee on Graduate Studies
Department of Ocean Engineering

Accepted by .....
Ain A. Sonin
Chairman, Departmental Committee on Graduate Studies
Department of Mechanical Engineering

System Identification and Control of an Arleigh Burke Class Destroyer Using an Extended Kalman Filter

by

Michael Eric Taylor

Submitted to the Departments of Ocean Engineering and Mechanical Engineering
on May 15, 2000, in partial fulfillment of the
requirements for the degrees of
Naval Engineer
and
Master of Science in Mechanical Engineering

Abstract

Maneuvering characteristics of surface combatants in the United States Navy are often ignored during the design process. Key maneuvering parameters such as tactical diameter and turning rate are determined during sea trials after the ship enters service. In the "Navy After Next", the study of maneuvering of surface combatants will become increasingly more important in efforts to reduce the number of personnel required to operate the ship and thus reduce life cycle costs. This thesis attempts to address this issue.

The thesis presents an Extended Kalman Filtering (EKF) algorithm to estimate the linear damping hydrodynamic coefficients for an Arleigh Burke Class Destroyer. Actual data is generated by conducting maneuvers (with a nonlinear model of the ship developed in a separate study) where nonlinear effects are small. The EKF then uses that data to estimate the hull stability coefficients (Y_v, N_v, Y_r, and N_r) on-line in real time. The coefficient values determined by the EKF are then used in a simulation model and the results are compared to the actual trajectories. Despite the nonlinearities present in the actual data, the EKF provides coefficient values that reproduce trajectories with only 15% error.

The linear coefficients are then used to develop simple controllers to automate maneuvering for the actual ship. The parameters determined by the EKF are used to derive a linear time invariant (LTI) model of the ship. This LTI model then serves as the basis for model-based compensator designs to automatically control ship maneuvers. The first controller is an autopilot to regulate the ship's heading and the second is a regulator that ensures the ship remains on its intended track. The performance of the compensators is then evaluated by simulating the performance of the LTI controllers on the nonlinear plant.

Thesis Supervisor: Michael S. Triantafyllou
Title: Professor of Hydrodynamics and Ocean Engineering

Acknowledgements

I would like to thank first and foremost my loving wife Laura. Her patience and kind understanding during my time here can not be overstated.

I would especially like to thank Franz Hover. He often helped me see the forest in spite of the trees. I would also like to thank Professor Michael Triantafyllou for inspiring my interest in the maneuvering and control of surface and underwater vehicles through his excellent course at MIT that bears the same name.

Finally, I sincerely appreciate the United States Navy for allowing me the honor and the opportunity to study at MIT.

Contents

List of Figures

List of Tables

Chapter 1

Introduction

1.1 Background

In the present naval ship design environment, reduced manning represents the cornerstone of any design. Manning reductions significantly reduce the life cycle cost of the project, which is the main goal given today's shrinking defense budgets. Reduced manning also implies fewer sailors being placed in harm's way during battle as well as enhanced quality of life. Reducing manning, however, affects nearly all aspects of a ship: maintenance, firefighting and damage control, maneuvering, etc. The solution to this problem requires a major paradigm shift from the Navy's current doctrine, culture, tradition, and training procedures.

Naval ships must operate in a multitude of different environments and perform well in each. Maneuvering of the ship in each of these environments currently requires numerous watchstanders on the bridge and in the Combat Information Center (CIC) during normal operations. Of these numerous watchstanders, one must be the helmsman, the individual responsible for manipulating the rudder and engines to keep the ship on its desired course and speed. With the advances in modern control theory and computing power, the functions performed by many of these watchstanders may potentially be automated. This represents a major change in current Navy operational doctrine, however.

Automation of these functions requires some method of automatic control. The evolution of control can be broken into two distinct periods. The period prior to 1957 can be considered the "Classical" period and the period from 1957 to the present can be considered the "Modern" period [33]. Classical control theory deals mainly with single-input/single-

output (SISO) linear time-invariant (LTI) systems, whereas modern control theory expands that capability to deal with multiple-input/multiple-output (MIMO) systems.

Automated ship maneuvering has been attempted since the invention of the gyroscope by E. A. Sperry in 1910. Sperry applied his gyroscope to the stabilization and steering of ships and later aircraft [33] using classical control methodology. Maneuvering of naval surface combatants, however, is almost completely neglected in the design process. Naval architects are content to accept the ship's maneuvering capabilities as determined by full-scale sea trials after the ship has been built. The manning goal of the USN's 21^{st} century surface combatant (DD-21) is 95 personnel. Automation of maneuvering must surely be employed in the design if this goal is to be realized.

1.2 Objectives

The main objective of this work is to apply a system identification technique known as the State Augmented Extended Kalman Filter (SAEKF) to identify the hydrodynamic coefficients of a model of the DDG-51 on-line in real time from noisy measurement data. The data obtained from the identification may then be used to develop simple controllers that can be tested during the design process for implementation on the full-scale ship. It is worth noting that the simulations performed in this study may not match full-scale DDG-51 trial data. The model used in this study to generate the ship maneuvering data was developed in [43]. No attempt has been made to validate this model against full-scale maneuvering data. The goal is to properly identify coefficients in an assumed form of the maneuvering equations and attempt to reproduce the states and trajectories produced by the model from [43]. In terms of developing control laws, the most important factor is the values of the system states, rather than exact values of the hydrodynamic coefficients for a particular ship. In fact, linear control systems often perform quite well despite errors as large as 40% in the states. Therefore, if the identified coefficients produce values of the system states that are close to those generated by the model in [43], that form of the simulation equations can be assumed to be accurate and may then be used to develop control laws to automate the ship's maneuvering.

In order to achieve the goal, a form of the simulation equations for ship maneuvering must be assumed. This form is then used to develop an SAEKF algorithm that accepts noisy

measurement data from ship maneuvers generated by the model in [43] and estimates the value of the hydrodynamic coefficients in an attempt to make the output of the simulation model match the actual measured data. The form of the model is based upon physical principles and contains the salient terms required to describe the coupled surge, sway, and yaw motions of the ship. Dimensionless quantities are employed throughout the process to maintain generality and ensure numerical stability of the algorithm.

The identification portion of the study limits its focus to forward motions in deep, calm seas with no current. The controller simulations, however, relax this condition and use currents and waves as disturbances to test the performance of the controller designs.

1.3 Contributions

This work describes and evaluates a process by which coefficients in maneuvering equations of motion can be identified on-line in real time. From these identified parameters, control laws for automating the ship's maneuvering in real time in the ship's operational environment can be developed. This method can be utilized early in the design process on scale models to determine the effectiveness of the automatic control systems and determine changes that need to be made. This work can be extended to apply to future naval combatant ship designs such as DD-21.

This work introduces a method by which naval architects can address maneuvering characteristics early in the design process and develop automatic controllers to reduce the number of human interfaces required to maneuver the ship. The method is written entirely in the MATLAB computing environment. This work will also help to provide Ocean Engineering graduate students at MIT with practical experience in guidance and control of ocean vehicles through its potential future implementation on a scale model. Further, the simulations developed in the thesis may be used as the basis for future student design projects in ship maneuvering and control.

1.4 Outline

Chapter two presents a truncated derivation of the governing equations for the SAEKF algorithm. It then presents an application of the identification process to a very large crude carrier (VLCC) Esso Osaka. This is an application of the significant work conducted

by Professor Martin Abkowitz of MIT in the late 1970's and early 1980's. This model is developed and used for verification of filter operation throughout the remainder of the thesis.

Chapter three presents a brief description of the United States Navy's Arleigh Burke Class (DDG-51) Destroyer. It then develops the governing equations of ship motion in the horizontal plane. The chapter concludes by developing the assumed form of the equations of motion to be employed in the SAEKF.

Chapter four develops the linear equations of ship maneuvering motion. It describes the results of the initial identification efforts and problems encountered. The chapter further describes bias and divergence in the Kalman Filter and some of the causes of these phenomena. The methods of addressing the problems encountered are then described. The chapter concludes with the results of the successful identification of the linear damping hydrodynamic coefficients for the DDG-51.

Chapter five briefly describes the theory of controller design by loopshaping. Two simple controllers are then designed using loopshaping and the linear models produced through the system identification efforts. The first controller is an autopilot designed to maintain the ship's actual heading about a slowly-varying reference value. Simulations of the controller are performed on the nonlinear plant to determine its performance. Cross-track errors evidenced in the autopilot design then lead to the design of a simple track-keeping controller. Simulations are performed on the nonlinear plant for this design as well.

Chapter six summarizes the work accomplished in the thesis and gives recommendations for future studies.

Chapter 2

System Identification and the State Augmented Extended Kalman Filter

This chapter introduces the use of the Extended Kalman Filter (EKF) in system identification. The governing equations of the EKF appear along with a brief description of the noise processes. The chapter concludes with an example application of the EKF to the identification of unknown hydrodynamic coefficients for the very large crude carrier (VLCC) Esso Osaka.

2.1 System Identification

System Identification (SI) is the process of developing or improving a mathematical representation of a physical system using experimental data. This process usually assumes a form of a model for a physical system and adjusts the unknown parameters in that model to fit physical data collected from the system in question. The State Augmented Extended Kalman Filter (SAEKF) illustrates one technique for performing SI. The system state vector is augmented with the system's unknown parameters and estimated as data is collected from the physical system.

Many methods exist for performing SI on mathematical models of physical systems. Several of these methods have been successfully applied to the ship maneuvering problem.

Maximum Likelihood Parameter Estimation was successfully applied in [41] to identify linear coefficients. Reference [13] covers several other methods such as Indirect Model Reference Adaptive System, Continuous Least Squares Estimation, and Recursive Least Squares Estimation. Abkowitz [3] successfully applied the SAEKF method to tanker ships in the early 1980's. The SAEKF method provides a means to update a system model on-line in real time. The success of the work presented in [3], coupled with the real time estimation capability, forms the basis for the choice of the SAEKF method in this study.

2.2 The Extended Kalman Filter

In the most general case, nonlinear systems and subsequent sets of discrete measurements of those systems can be described by a set of nonlinear, stochastic differential equations of the following form [1]:

$$\dot{\underline{x}}(t) = \mathbf{f}(\underline{x}(t), t) + \underline{w}(t) \tag{2.1}$$

$$\underline{z}_k = \mathbf{h_k}(\underline{x}(t_k)) + \underline{v}_k \tag{2.2}$$

where:

$\underline{x}(t)$ represents the system state vector,

$\mathbf{f}(\underline{x}(t), t)$ represents the system description matrix,

$\underline{w}(t)$ represents a zero-mean Gaussian sequence with covariance matrix $\mathbf{Q}(t)$,

$\underline{z}_k$ represents the measurement vector,

$\mathbf{h_k}(\underline{x}(t_k))$ represents the measurement description matrix, and

$\underline{v}_k$ represents a zero-mean Gaussian sequence with covariance matrix $\mathbf{R_k}$.

In the ship maneuvering problem, system measurements typically consist of direct measurements of the state variables. Thus, the matrix $\mathbf{h_k}(\underline{x}(t_k))$ reduces to a constant identity matrix. For example, ships often utilize a Global Positioning System (GPS) to directly measure the ship's position and speed. The ship also has a gyrocompass to directly measure the instantaneous heading angle. The direct state measurements require no additional calculations to determine the value of the state. Therefore, the system measurement matrix

[1] The derivations that follow appear in more detail in [19].

reduces to a constant function equal to the identity matrix.[2] Keeping this fact in mind, equation 2.2 reduces to the following:

$$\underline{z}_k = \mathbf{h_k}\underline{x}(t_k) + \underline{v}_k \tag{2.3}$$

The equation of motion 2.1 and the measurement equation 2.3 now govern the dynamics of the entire system. The EKF method seeks the minimum variance estimate of $\underline{x}(t)$ as a function of time and the measurement data accumulated up to time t_k. The sequel presents an abbreviated derivation of the theory behind the EKF algorithm. Reference [19] presents a more detailed derivation of the intermediate steps.

2.2.1 Process and Sensor Noise

The noise sequences $\underline{w}$ and $\underline{v}_k$ in equations 2.1 and 2.3 represent the process and sensor noise, respectively. Their properties and associated covariance matrices have yet to be addressed.

In the ship maneuvering problem, the process noise represents the uncertainty in the assumed form of the model as well as uncertainty in predicting external disturbances. For example, the sea may not always exhibit a wave spectrum exactly consistent with that predicted by statistical data. In calm seas, however, this uncertainty is removed and only the uncertainty in the model form remains. Thus, the process noise covariance may be assumed to be constant. This is not a limitation, however, because even in a high sea state, the additional uncertainty due to the wave excitation will vary slowly over time and can be considered piecewise constant [32]. Furthermore, because the process noise represents uncertainty, it is assumed that the state vector and process noise are independent and uncorrelated random variables.

The sensor noise represents the uncertainty in the measurements. For example, GPS systems available in the commercial market provide position information to within +/- 100 feet in some instances, but not the exact location. The measurement model must address this uncertainty. Therefore, in the sequel, the following assumptions hold for the process and sensor noise:

[2] If all state variables are not measured, the matrix will consist of ones and zeros of sufficient size to perform the required linear algebraic operations.

1. White noise processes.[3]

   • The ship motions are slow compared to the dynamics of waves, structural vibrations, etc. Thus, the time constant of the process noise is much, much faster than the time constant of the ship motions.

   • The observation interval must be long compared to the correlation time of the sensor noise. Typical shipboard sensors exhibit the capability of sampling rates as high as 100 hertz. Therefore, a sampling interval of not less than one second meets this condition and is more than adequate to fully capture the slow ship motion dynamics.

2. Independent, uncorrelated, zero-mean, Gaussian random variables (denoted N(0,Q)). Thus, $E\left[\underline{w}(t)\underline{v}_k^T\right] = E\left[\underline{v}_k\underline{w}(t)^T\right] = 0$ for all k and t.

3. Covariances are constant or piecewise constant varying slowly with time.

These assumptions are quite important in the derivations that follow. Reference [19] provides a more detailed discussion of the noise processes.

2.2.2 State Estimate and Error Covariance Propagation

The EKF method seeks to minimize the error of the estimate in some statistical sense as a function of time. Thus, the error obviously depends on time. Define the error, $\tilde{\underline{x}}(t)$, and its associated error covariance matrix, $\mathbf{P}(t)$ as follows:

$$\tilde{\underline{x}}(t) \equiv \hat{\underline{x}}(t) - \underline{x}(t) \tag{2.4}$$

$$\mathbf{P}(t) \equiv E[\tilde{\underline{x}}(t)\tilde{\underline{x}}(t)^T] \tag{2.5}$$

where $\hat{\underline{x}}(t)$ denotes the minimum variance estimate determined by the EKF, and $E[\ \bullet\ ]$ denotes the expectation operator. From the definitions in equations 2.1, 2.4, and 2.5, it can be shown [19] that equations 2.6 and 2.7 govern the state estimate and its associated error covariance propagation. Equation 2.7 omits the time dependence of $\mathbf{f}$ and $\underline{x}$ for notational

[3]Nature does not exhibit white noise processes. Thus, the white noise assumption is only valid subject to the conditions presented.

convenience.

$$\dot{\hat{\underline{x}}}(t) = \hat{\mathbf{f}}(\underline{x}(t), t) \tag{2.6}$$

$$\dot{\mathbf{P}}(t) = \widehat{\underline{x}\mathbf{f}^T} - \hat{\underline{x}}\hat{\mathbf{f}}^T + \widehat{\mathbf{f}\underline{x}^T} - \hat{\mathbf{f}}\hat{\underline{x}}^T + \mathbf{Q}(t) \tag{2.7}$$

In order to solve these equations, $\widehat{\mathbf{f}}$ must be known at each instant. The value of $\widehat{\mathbf{f}}$, however, depends upon the entire probability density function of $\underline{x}$ at each instant of time as shown by the following relation:

$$\hat{\underline{\mathbf{f}}}(\underline{x}, t) = \int_{-\infty}^{\infty} \cdots \int_{-\infty}^{\infty} \underline{\mathbf{f}}(\underline{x}, t) p(\underline{x}, t)\, dx_1 \ldots dx_n \neq \underline{\mathbf{f}}(\hat{\underline{x}}, t) \tag{2.8}$$

where $p(\underline{x}, t)$ denotes the probability density function of $\underline{x}$. Practical algorithms require methods of computing $\underline{x}$ and $\mathbf{P}$ without knowing $p(\underline{x}, t)$. One method of accomplishing this is by expanding $\mathbf{f}$ in a Taylor series about the current estimate, $\hat{\underline{x}}$, as follows (assuming the required derivatives exist):

$$\mathbf{f}(\underline{x}, t) = \mathbf{f}(\hat{\underline{x}}, t) + \left.\frac{\partial \mathbf{f}}{\partial \underline{x}}\right|_{\underline{x}=\hat{\underline{x}}} (\underline{x} - \hat{\underline{x}}) + \cdots \tag{2.9}$$

Truncating equation 2.9 to include only the first order terms, taking the expected value, and substituting into equations 2.6 and 2.7, yields the following approximate expressions for the propagation of the estimated state vector and its associated error covariance:

$$\dot{\hat{\underline{x}}} = \mathbf{f}(\hat{\underline{x}}, t) \tag{2.10}$$

$$\dot{\mathbf{P}}(t) = \mathbf{F}(\hat{\underline{x}}, t)\mathbf{P}(t) + \mathbf{P}(t)\mathbf{F}^T(\hat{\underline{x}}, t) + \mathbf{Q}(t) \tag{2.11}$$

where $\mathbf{F}(\hat{\underline{x}}, t)$ is the matrix whose ij^{th} element is defined as follows:

$$f_{ij} \equiv \left.\frac{\partial f_i(\underline{x}, t)}{\partial x_j}\right|_{\underline{x}=\hat{\underline{x}}} \tag{2.12}$$

2.2.3 State Estimate Update, Error Covariance Update, and the Kalman Gain Matrix

The filtering equations 2.10 and 2.11 propagate the state estimate and error covariance over the time period between measurements ($t_{k-1} \leq t < t_k$). Therefore, to complete the

filter and update the state estimate for the next time step, the actual state measurement must be taken into account. Because the EKF algorithm produces a minimum variance estimate of the state vector, there will likely be a difference between the propagated state estimate (denoted $\underline{\hat{x}}_k(-)$ [4]) and the actual measurement (denoted $\underline{z}_k$). Thus, the updated state estimate (denoted $\underline{\hat{x}}_k(+)$) can be computed by a linear combination of the propagated state estimate and the difference between the actual measurement and propagated state estimate. The scaling factor in this linear combination is known as the Kalman Gain matrix, $\mathbf{K_k}$. Equation 2.13 illustrates this relation.

$$\underline{\hat{x}}_k(+) = \underline{\hat{x}}_k(-) + \mathbf{K_k}[\underline{z}_k - \widehat{\mathbf{h_k}}(\underline{x}_k(-))] \tag{2.13}$$

Measurements affect the error covariance in a manner similar to the state estimate update. Therefore, denote the propagated error covariance as $\mathbf{P_k}(-)$ and the updated error covariance as $\mathbf{P_k}(+)$. The optimum Kalman Gain matrix, $\mathbf{K_k}$, minimizes the error covariance update, $\mathbf{P_k}(+)$. Expressing $\mathbf{P_k}(+)$ as a function of of $\mathbf{K_k}$ yields the following expression to be minimized:

$$\mathbf{P_k}(+) = \mathbf{P_k}(-) + \mathbf{K_k} E\left[[\underline{z}_k - \widehat{\mathbf{h_k}}(\underline{x}_k)]\underline{\tilde{x}}_k(-)^T\right] \tag{2.14}$$

Like the state estimate update, $\underline{\hat{x}}_k(+)$, equation 2.14 is a linear combination of the propagated error covariance and the estimation error. Minimizing equation 2.14 yields the following expression for the optimum Kalman Gain matrix (see [19] for details):

$$\mathbf{K_k} = -E\left[\underline{\tilde{x}}_k(-)[\underline{z}_k - \widehat{\mathbf{h_k}}(\underline{x}_k)]^T\right]\left\{E\left[[\underline{z}_k - \widehat{\mathbf{h_k}}(\underline{x}_k)][\underline{z}_k - \widehat{\mathbf{h_k}}(\underline{x}_k)]^T\right] + \mathbf{R_k}\right\}^{-1} \tag{2.15}$$

Note that $\widehat{\mathbf{h_k}}$ depends upon the entire probability density function of $\underline{x}(t)$ similar to $\hat{\mathbf{f}}$ in 2.2.2.[5] Employing the method in 2.2.2 and expanding $\mathbf{h_k}$ in a Taylor series about the current propagated state estimate, $\underline{\hat{x}}_k(-)$, yields the following expression:

$$\underline{z}_k = \mathbf{h_k}(\underline{\hat{x}}_k(-)) + \mathbf{H_k}(\underline{\hat{x}}_k(-))(\underline{x}_k - \underline{\hat{x}}_k(-)) + \cdots \tag{2.16}$$

[4] $\underline{\hat{x}}_k(-)$ and $\mathbf{P_k}(-)$ represent the solutions to equations 2.10 and 2.11 on the interval $t_{k-1} \leq t < t_k$.
[5] See equation 2.8.

where:

$$\mathbf{H_k}(\underline{\hat{x}}_k(-)) \equiv \left.\frac{\partial \mathbf{h_k}(\underline{x})}{\partial \underline{x}}\right|_{\underline{x}=\underline{\hat{x}}_k(-)} \tag{2.17}$$

Thus, similar to $\mathbf{F}$, $\mathbf{H_k}$ is a matrix whose ij^{th} element is given by the following expression:

$$(\mathbf{H_k})_{ij} \equiv \left.\frac{\partial (\mathbf{h_k})_i(\underline{x}_k)}{\partial (x_k)_j}\right|_{\underline{x}_k=\underline{\hat{x}}_k(-)} \tag{2.18}$$

Truncating equation 2.16 after two terms, taking the expected value and substituting into equations 2.13, 2.14, and 2.15 yields the Extended Kalman Filter update equations:

$$\underline{\hat{x}}_k(+) = \underline{\hat{x}}_k(-) + \mathbf{K_k}[\underline{z}_k - \mathbf{h_k}(\underline{\hat{x}}_k(-))] \tag{2.19}$$

$$\mathbf{K_k} = \mathbf{P_k}(-)\mathbf{H_k}^T(\underline{\hat{x}}_k(-))\left[\mathbf{H_k}(\underline{\hat{x}}_k(-))\mathbf{P_k}(-)\mathbf{H_k}^T(\underline{\hat{x}}_k(-)) + \mathbf{R_k}\right]^{-1} \tag{2.20}$$

$$\mathbf{P_k}(+) = [\mathbf{I} - \mathbf{K_k}\mathbf{H_k}(\underline{\hat{x}}_k(-))]\mathbf{P_k}(-) \tag{2.21}$$

Figures 2-1 and 2-2 illustrate the process with a flowchart and timing diagram. Table 2.1 presents a summary of the Extended Kalman Filter algorithm. Each block in the flowchart represents a section from Table 2.1. Figures 2-1 and 2-2 should be used in conjunction with Table 2.1 to illustrate the flow of the algorithm and the governing equations for each stage of the process.

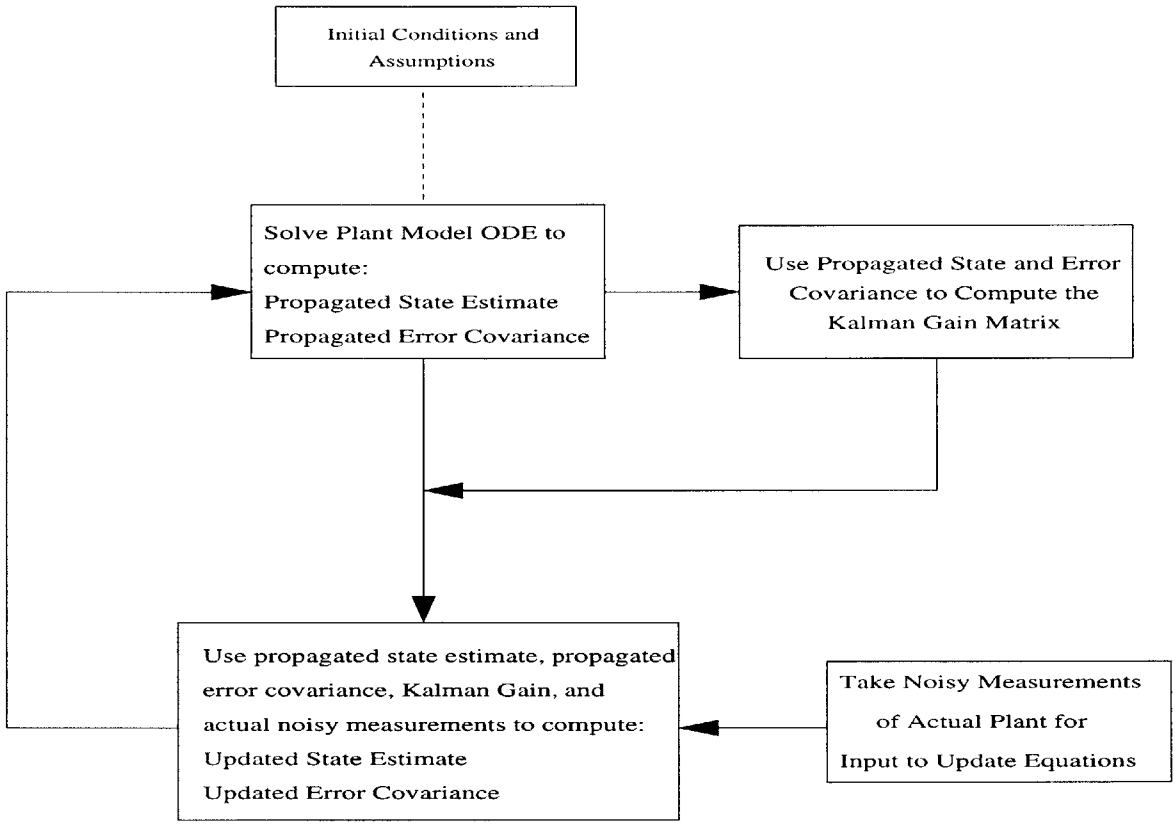

Figure 2-1: EKF Algorithm Flowchart

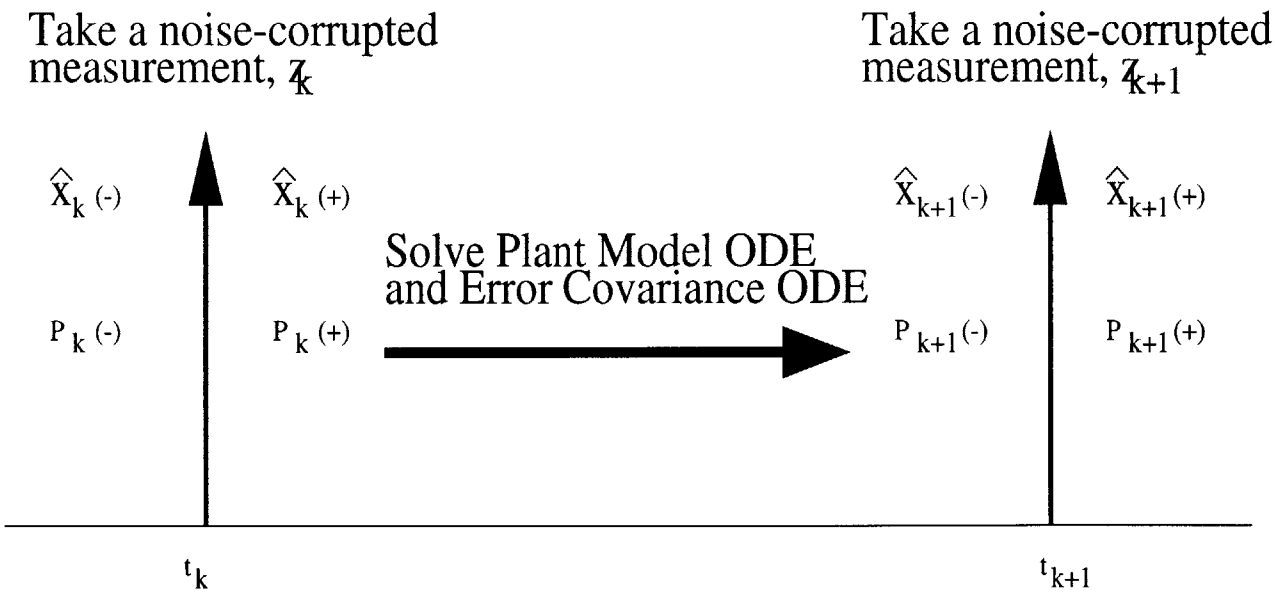

Figure 2-2: EKF Timing Diagram Adapted from Figure 4.2-1 of [19]

Table 2.1: Summary of the Extended Kalman Filter Equations

System Model	$\dot{\underline{x}}(t) = \mathbf{f}(\underline{x}(t), t) + \underline{w}(t)$
Measurement Model	$\underline{z}_k = \mathbf{h_k}(\underline{x}(t_k)) + \underline{v}_k$
Initial Conditions	$\underline{x}(0) \sim N(\hat{\underline{x}}_0, \mathbf{P_0})$
Other Assumptions	$E\left[\underline{w}(t)\underline{v}_k^T\right] = 0 \ \forall$ k and t
State Estimate Propagation	$\dot{\hat{\underline{x}}} = \mathbf{f}(\hat{\underline{x}}, t)$ (Plant Simulation Model)
Error Covariance Propagation	$\dot{\mathbf{P}}(t) = \mathbf{F}(\hat{\underline{x}}, t)\mathbf{P}(t) + \mathbf{P}(t)\mathbf{F}^T(\hat{\underline{x}}, t) + \mathbf{Q}(t)$
State Estimate Update	$\hat{\underline{x}}_k(+) = \hat{\underline{x}}_k(-) + \mathbf{K_k}[\underline{z}_k - \mathbf{h_k}(\hat{\underline{x}}_k(-))]$
Error Covariance Update	$\mathbf{P_k}(+) = [\mathbf{I} - \mathbf{K_k}\mathbf{H_k}(\hat{\underline{x}}_k(-))]\mathbf{P_k}(-)$
Kalman Gain	$\mathbf{K_k} = \mathbf{P_k}(-)\mathbf{H_k}^T(\hat{\underline{x}}_k(-))\mathbf{S}^{-1}(\hat{\underline{x}}_k(-))$
Definitions	$\mathbf{F}(\hat{\underline{x}}(t), t) \equiv \frac{\partial \mathbf{f}(\underline{x}(t), t)}{\partial \underline{x}(t)}\Big\|_{\underline{x}(t)=\hat{\underline{x}}(t)}$
	$\mathbf{H_k}(\hat{\underline{x}}_k(-)) \equiv \frac{\partial \mathbf{h_k}(\underline{x})}{\partial \underline{x}}\Big\|_{\underline{x}=\hat{\underline{x}}_k(-)}$
	$\mathbf{S}(\hat{\underline{x}}_k(-)) \equiv \left[\mathbf{H_k}(\hat{\underline{x}}_k(-))\mathbf{P_k}(-)\mathbf{H_k}^T(\hat{\underline{x}}_k(-)) + \mathbf{R_k}\right]$

Adapted from Table 6.1-1 of [19]

2.3 System Identification of the Esso Osaka

No a priori information on the parameters of the DDG-51 was available in this study. Thus, if the identification process produced erroneous values of the coefficients, there would be no definitive method of isolating the problem to the model or the filter. In an effort to ensure proper operation of the filter prior to use in identifying the DDG-51 hydrodynamic coefficients, a linear model of the Esso Osaka was developed using coefficient values provided in [3].

The Esso Osaka is a 280,000 dead-weight-ton VLCC with principal characteristics listed in Table 2.2. Abkowitz conducted a series of experiments outlined in [3] in the late 1970's

Table 2.2: Esso Osaka Principle Characteristics

LBP	1066.3 ft
Beam	173.9 ft
Draft	92.8 ft
A_r (rudder area)	1289.67 ft^2
AR (rudder aspect ratio)	1.538
Δ	314,410 lton
LCG (aft of midship)	25 ft

and early 1980's to evaluate the EKF technique as a candidate for identification of ship hydrodynamic derivatives. The study produced favorable results and simulations using the identified coefficients matched the full-scale data quite well. The successful results presented in [3] formed the basis for choosing the EKF method in this study.

The mathematical calculations involved in formulating the EKF are quite involved. The potential for error, therefore, is rather high. Thus, in order to ensure that no mathematical errors had occurred, it was necessary to test the filter against a dynamical model with known parameters. Successful operation of the filter in identifying the known parameter values would indicate that the filter had been properly formulated. The values of the coefficients appear in Table 2.3. The negative signs have been included in the coefficient definitions of Y_v and N_v to follow the convention outlined in [49].

Table 2.3: Esso Osaka Nondimensional Hydrodynamic Coefficients

$-Y_v$	0.0244
$(m - Y_r)$	0.0138
$-N_v$	1.4578e-3
$(mx_g - N_r)$	8.093e-4

The results of the identification appear in Figures 2-3 and 2-4. These figures clearly indicate that the filter operates correctly. Notice how the parameter estimates converge to the exact values of the actual coefficients over time in Figure 2-4. This is indicative of the fact that the dynamical model in the filter is identical to the dynamical model producing the measurements. The fact that there are no modeling errors removes the requirement for process noise (i.e. $\mathbf{Q} = 0$). Thus, the filter trusts its own state estimates and converges quickly to the proper values based upon the initial measurements. Figure 2-3 shows how the estimates of the physical states converge immediately. This is due to the exact dynamical model in the filter and the fact that each of the four physical states are measured. Figure 2-4 indicates that each of the parameter estimates requires about 3 minutes to converge. This is because each of these states must be estimated by the filter and some dynamic information is required before the filter can produce good estimates. After about three minutes, the error between the actual and estimated state vectors has decayed to zero. Thus, the computed gains are very small and the filter has effectively "learned" the dynamics of the system and no longer requires measurement information to produce good estimates.

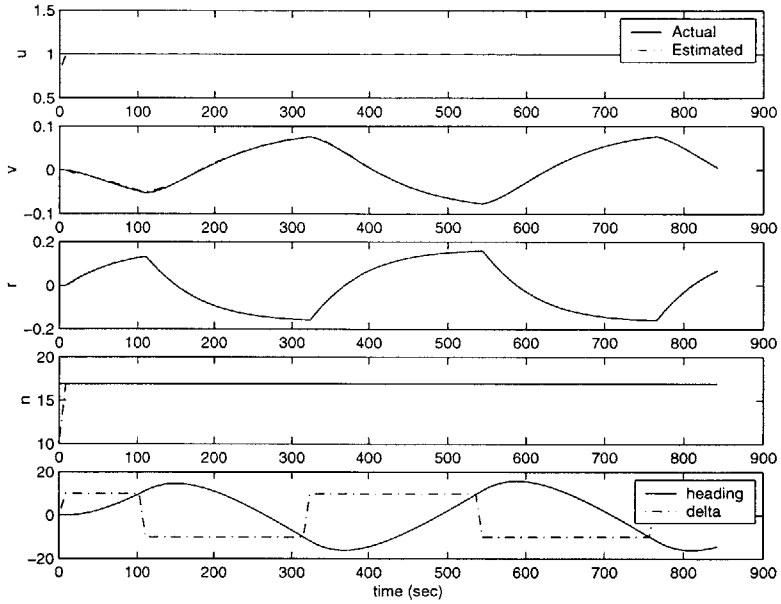

Figure 2-3: State Estimates of the Esso Osaka During a $10^o/10^o$ Zig-Zag Maneuver

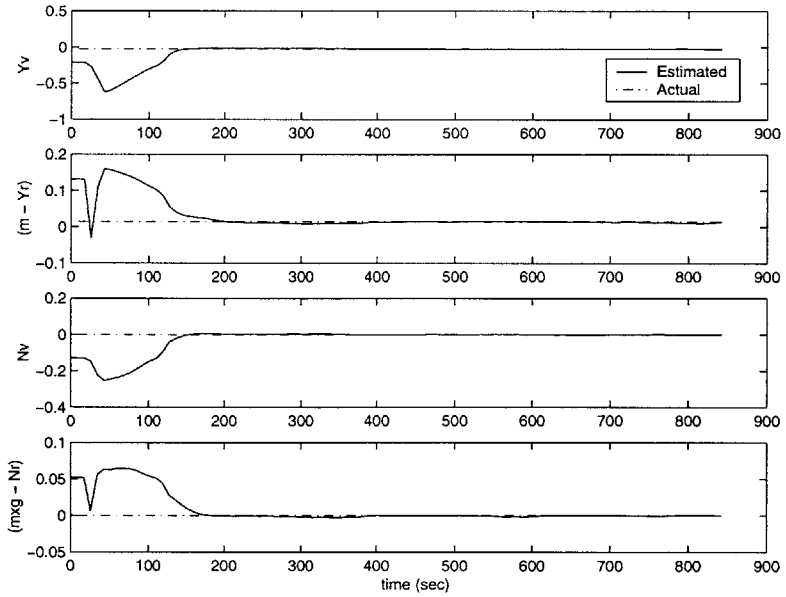

Figure 2-4: Parameter Estimates of the Esso Osaka During a $10^o/10^o$ Zig-Zag Maneuver

Results of simulations performed using the identified coefficients appear in Figures 2-5 and 2-6. The identified coefficients reproduce the states and trajectory with very small error. This, again, can be attributed to the fact that the filter contained an exact dynamical model during the identification process. Note also that the trajectory shown in Figure 2-6 is identical to the maneuver used to identify the coefficients.

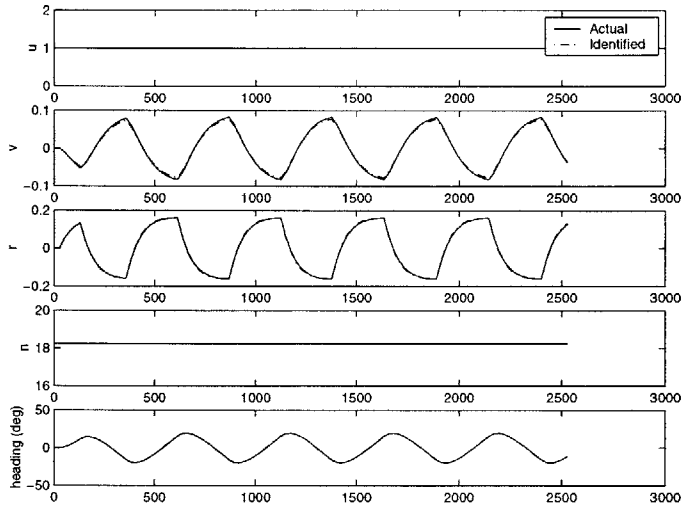

Figure 2-5: Simulated States of the Esso Osaka During a $10^o/10^o$ Zig-Zag Maneuver

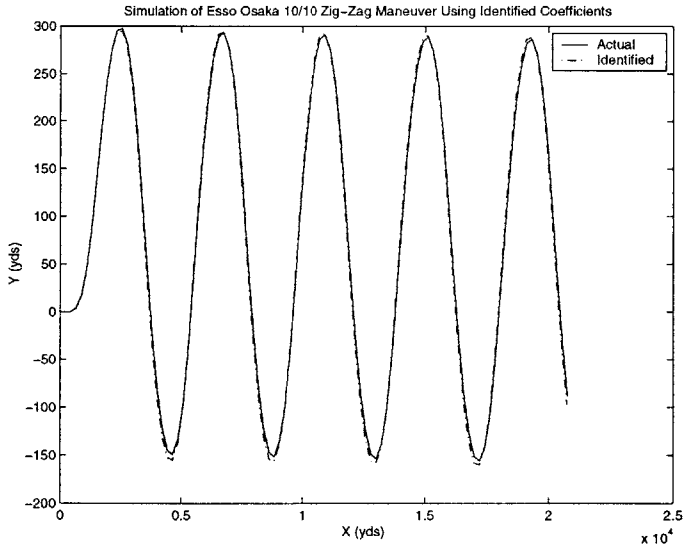

Figure 2-6: Simulated Trajectory of the Esso Osaka During a $10^o/10^o$ Zig-Zag Maneuver

Figure 2-7 shows the simulation results in a 10^o steady turn maneuver. The simulation results are still quite accurate despite the differing maneuver. The error shown in the figure is less than 5% in the turning diameter. The error can most likely be attributed to roundoff errors in determining the coefficient values. This small error, however, is certainly ideal for control system design.

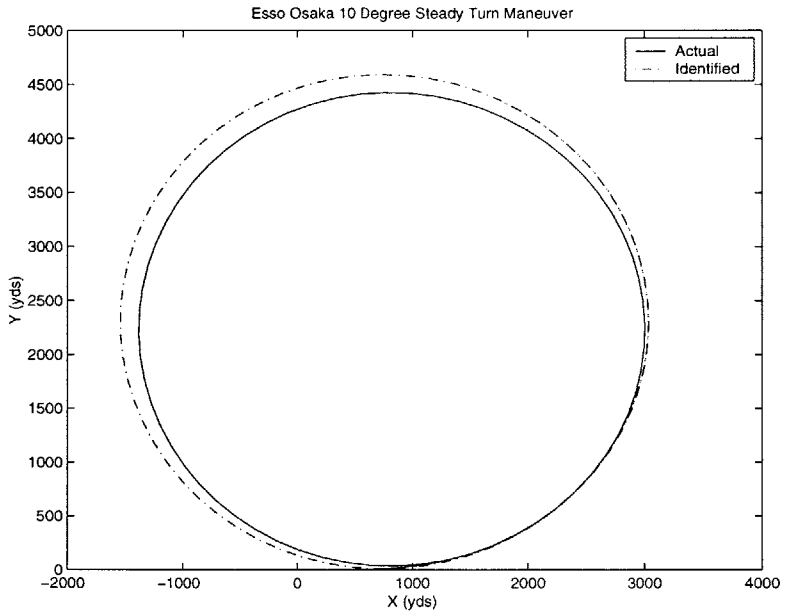

Figure 2-7: Simulated Trajectory of the Esso Osaka During a 10^o Rudder Steady Turn

Chapter 3

Nonlinear Simulation Model

Many of the intricate details of the hullform described in the sequel have been omitted. This work uses a model developed in [43] to generate the data for the full-scale ship. Classification restrictions prevent verification of this model against any full-scale data for the DDG-51. Thus, no attempt has been made here to do so. The focus of this work lies in using the SAEKF process to identify the unknown parameters in the equations of motion and develop control systems based upon the identified parameters. The goal then becomes using the identified values of the parameters to reproduce ship trajectories generated by the model from [43].

The sequel develops the general equations of rigid-body motion and the assumed form of the simulation model to be used in the SAEKF. Note that the form of the simulation equations developed in this study are in no way related to the form of the equations used in [43]. This ensures that the SAEKF does not merely estimate the parameters of a model identical to that which it contains. In fact, the form of the simulation equations is unimportant as long as the trajectory of the actual data is reproduced. Thus, the issue of coefficient cancellation described in [3] becomes moot. The goal of this study is not to identify individual coefficient values, but to reproduce trajectories. This implies that the forces and moments have been adequately modeled, which is the most important factor in control system design.

3.1 The Arleigh Burke Class Destroyer

The United States Navy (USN) Arleigh Burke (DDG-51) Class destroyer represents the state of the art in operational warships today. It is a twin-screw vessel powered by four

LM2500 gas turbine engines coupled to controllable-reversible pitch (CRP) propellers. The vessel has a wider beam than conventional warships, but is still considered to have fine lines. Table 3.1 lists the ship's principal characteristics. The vessel uses two mechanically-linked rudders located downstream of the propellers to maintain course control. The ship's propellers maintain 100% pitch for all speeds above approximately 10 knots, and thus will be considered fixed for the duration of this study. The ship has port-starboard symmetry as do nearly all ships in existence today.

Table 3.1: DDG-51 Principal Characteristics

Length (LBP)	466 ft
Beam (B)	59 ft
Draft (T)	21 ft
Displacement (Δ)	8500 lton
Waterplane Area (A_w)	29896 ft^2
Long Ctr Gravity (LCG)	2.8 ft aft midship
Block Coeff (C_b)	0.522
Prismatic Coeff (C_p)	0.615

3.2 Governing Equations of Motion

3.2.1 Rigid-Body Inertial Forces and Moments

The following sections develop the equations governing the inertial forces and moments experienced by the body in dynamic motion. Simplifications ultimately reduce the generalized equations to only those governing motions in the horizontal plane.

3.2.1.1 Generalized Equations of Rigid-Body Motion

The complete derivation of the generalized equations of motion for a rigid body moving on the surface of the earth begins by choosing an inertial coordinate system with its origin located at the earth's center of gravity. This is necessary to account for centrifugal forces, coriolis forces, etc. The body experiences these forces due to the earth's gravitational field and its relative linear and angular velocity to that of the body. The effects of these phenomena, however, can be considered small (and thus neglected) for large objects such as ships. Reference [2] details this portion of the derivation, so it will not be reproduced

here.

Based upon the assumptions outlined in [2], the coordinate system is transformed into a body-fixed reference frame with its origin located at the midship section. Figure 3-1 illustrates the coordinate system in a body-fixed reference frame.

In the most general case, the ship may exhibit coupled motions in all six degrees of freedom shown in Figure 3-1. All three forces and all three moments shown in Figure 3-1 act on the ship during normal operating conditions while underway at sea. Equating the forces and moments acting on the ship to the rates of change of linear and angular momentum experienced by the ship yields the generalized equations of motion shown in equations 3.1 through 3.6.

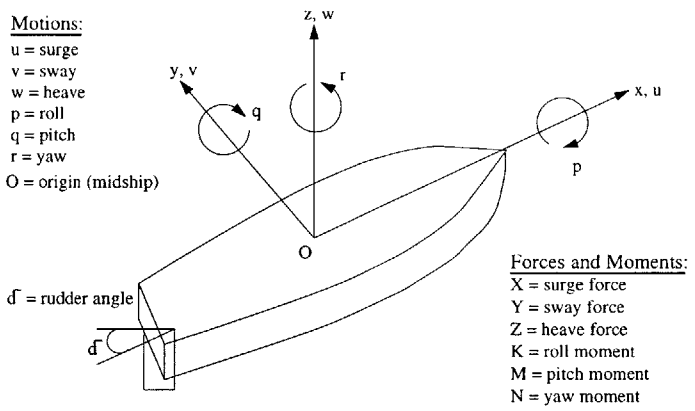

Figure 3-1: Body-Fixed Coordinate System

$$X = m\Big[\dot{u} + qw - rv - x_g(q^2 + r^2) + y_g(pq - \dot{r}) + z_g(pr + \dot{q})\Big] \tag{3.1}$$

$$Y = m\Big[\dot{v} + ru - pw - y_g(r^2 + p^2) + z_g(qr - \dot{p}) + x_g(qp + \dot{r})\Big] \tag{3.2}$$

$$Z = m\Big[\dot{w} + pv - qu - z_g(p^2 + q^2) + x_g(rp - \dot{q}) + y_g(rq + \dot{p})\Big] \tag{3.3}$$

$$K = I_x\dot{p} + (I_z - I_y)qr + m\Big[y_g(\dot{w} + pv - qu) - z_g(\dot{u} + ru - pw)\Big] \tag{3.4}$$

$$M = I_y\dot{q} + (I_x - I_z)rp + m\Big[z_g(\dot{u} + qw - rv) - x_g(\dot{v} + pv - qu)\Big] \tag{3.5}$$

$$N = I_z\dot{r} + (I_y - I_x)pq + m\Big[x_g(\dot{v} + ru - pw) - y_g(\dot{w} + qw - rv)\Big] \tag{3.6}$$

where m represents the mass of the body and I_x, I_y, and I_z represent the moments of inertia about the appropriate axis. Because the longitudinal center of gravity is sufficiently close to the origin, and the ship is nearly symmetric, the cross-coupling inertia terms can be considered small and neglected.

3.2.1.2 Equations of Motion in the Horizontal Plane

Despite the appearance of the tight coupling of all the motions in equations 3.1 through 3.6, motions in the horizontal plane exhibit weak coupling to the out-of-plane motions [37], [49]. Therefore, motion in the horizontal plane can be considered separately from motions out-of-plane. This simplification implies the following:

$$w = p = q = Z = K = M = 0 \tag{3.7}$$

For a ship with no list (the usual case), the transverse component of the center of gravity, y_g, must lie somewhere on the x-axis. Orthogonality of the coordinate system implies the following:

$$y_g = 0 \tag{3.8}$$

Substituting equations 3.7 and 3.8 into equations 3.1, 3.2, and 3.6 yields the equations of motion in the horizontal plane:

$$X = m\left[\dot{u} - rv - x_g r^2\right] \tag{3.9}$$

$$Y = m\left[\dot{v} + ru + x_g \dot{r}\right] \tag{3.10}$$

$$N = I_z \dot{r} + m\left[x_g(\dot{v} + ru)\right] \tag{3.11}$$

The right-hand sides of equations 3.9 through 3.11 describe the inertial forces and moments acting on the body during dynamic motion in the horizontal plane. The remaining derivations address the external forces that balance the inertial forces.

3.2.2 Balancing Forces and Moments

Many different forms for the equations governing the balancing forces and moments exist in the open literature. These models can be classified in three main categories [10]:

1. Input-Output models.
2. Holistic (regression) models.
3. Modular models.

Input-output models describe the direct effect of varying control parameters on the maneuvering response of the ship. Holistic models treat the ship as a complete entity with forces and moments described by a Taylor series expansion containing the pertinent kinematic and geometric parameters. Modular models treat all major contributing elements as separate, interactive modules which can be developed and tested separately. Developments over the last decade indicate that the flexibility of the modular approach makes it very attractive for future applications [10]. Thus, this type of approach has been adopted in this work.

The following sections develop the equations governing the forces and moments[1] which balance the inertial forces and moments derived in 3.2.1. The total force and moment can be subdivided into forces and moments resulting from the following modular contributions:

1. External influences (wind, waves, etc.), X_{ext}, Y_{ext}, N_{ext}.
2. Steady-state effects, X_0, Y_0, N_0.
3. Propulsive devices (propellers, thrusters, etc.), X_P, Y_P, N_P.
4. Rudder forces, X_R, Y_R, N_R.
5. Interactions between the fluid and the hull, X_f, Y_f, N_f.

Thus, the total forces and moments may be described by the following equations:

$$X = X_{ext} + X_0 + X_P + X_R + X_f \tag{3.12}$$

$$Y = Y_{ext} + Y_0 + Y_P + Y_R + Y_f \tag{3.13}$$

$$N = N_{ext} + N_0 + N_P + N_R + N_f \tag{3.14}$$

3.2.2.1 External Forces and Moments

This study considers maneuvering only in calm, deep water with no wind or current effects. This is not a likely operational environment for a full-scale ship. The goal of this study, however, is to reproduce maneuvering trajectories produced by the model developed in [43]. No environmental forces were considered in that study and therefore will not be considered here. Once the SAEKF method proves effective in the absence of environmental forces, the next logical step would be the addition of environmental forces to determine

[1] X, Y, and N from equations 3.9 through 3.11.

their effects. Therefore, X_{ext}, Y_{ext}, and N_{ext} are taken to be zero for the duration of the identification portion of this work. These effects will be considered, however, during simulation of controller designs. This is not a limitation because a scale model may be tested in a pool or tank where the environment can be carefully controlled to perform the identification.

3.2.2.2 Steady-State Effects

Steady-state effects consist of forces and moments present in steady-state motion. Thus, the steady-state X_0 is taken to be the ship resistance at the steady-state forward speed when all other dynamic terms are zero. Y_0 and N_0 represent steady-state sway force and yaw moment, respectively. These phenomena exist primarily on single-screw ships and manifest themselves through a tendency for the ship's stern to "walk" in a particular direction when the propeller thrust is small. DDG-51 has two shafts and two propellers that rotate in opposing directions. Thus, for this platform, the steady-state sway forces and yaw moments cancel and can be considered zero. Furthermore, because the steady-state forces and moments cancel, the dynamic forces and moments will cancel as well. Thus,

$$Y_0 = N_0 = Y_P = N_P = 0 \tag{3.15}$$

3.2.2.3 Propulsive Forces and Moments

When a ship propels itself through water, the longitudinal force must be equal to the difference between the hull resistance and the propeller thrust. The open-water thrust provided by the propeller can be expressed as follows [49]:

$$T_o = \rho n^2 D^4 \left[K_0 + K_1 J + K_2 J^2 \right] \tag{3.16}$$

$$J = \frac{(1-w)u}{nD} \tag{3.17}$$

where n represents the propeller speed, D represents the propeller diameter, and J represents the advance coefficient. The constants (K_0, K_1, and K_2) represent the coefficients in a parabolic fit of the thrust coefficient to the open-water propeller curve and $(1-w)$ represents the Taylor wake fraction. Inserting equation 3.17 into equation 3.16 and carrying out the

requisite algebra results in the following expression:

$$T_o = X_P = \eta_1 n^2 + \eta_2 nu + \eta_3 u^2 \tag{3.18}$$

where:

$$\eta_1 = \rho D^4 K_0 \tag{3.19}$$

$$\eta_2 = (1-w)\rho D^3 K_1 \tag{3.20}$$

$$\eta_3 = (1-w)^2 \rho D^2 K_2 \tag{3.21}$$

Modeling of propeller thrust and torque introduces an additional state variable, n, into the equations of motion. Appropriate models for this variable depend heavily upon the type of propulsion machinery the plant contains. The DDG-51 propulsion system consists of four LM2500 gas turbine engines mechanically coupled to two shafts via a set of reduction gears. Reference [49] recommends the following form for modeling a gas turbine propulsion system:

$$\dot{n} = \frac{\eta_r \lambda \eta_g Q_E - Q_P}{2\pi I_p} \tag{3.22}$$

where Q_E and Q_p represent the engine and propeller torque, respectively, I_p represents the polar moment of inertia for the entire engine/gear/shaft/propeller arrangement, λ represents the reduction gear ratio, and η_r and η_g represent the propeller relative rotative efficiency and reduction gear transmission efficiency, respectively. This model is intended only to adequately model the changes in propeller speed during maneuvers. It is not intended to completely capture the performance of the engine itself. Adequate modeling of propeller speed changes captures the salient dynamics required for maneuvering and trajectory simulation. Therefore, this model suffices for the task at hand. Thus, the engine model used in this study is the same as that used in [43] [2].

$$Q_E = Q_{max}\left[(af_r + b)\frac{n\lambda}{n_{max}} + cf_r\right] \tag{3.23}$$

$$Q_p = \rho n^2 D^5 K_Q(J) = \rho n^2 D^5 \left[Q_0 + Q_1 J + Q_2 J^2\right] \tag{3.24}$$

[2]Reference [1] provides a more detailed model to capture the performance of the engine.

where all coefficients in equation 3.23 are taken directly from [43], f_r represents the fuel rate, and the constants (Q_0, Q_1, and Q_2) represent the coefficients in a parabolic fit of the torque coefficient to the open-water propeller curve.

3.2.2.4 Rudder Forces and Moments

Modeling the rudder forces and moments is somewhat more complicated than the derivations presented thus far because the angle of attack decreases due to the sway and yaw motions. Figure 3-2 illustrates the coordinate system and vector diagrams of the rudder forces. The ultimate goal is to determine expressions for X_R and Y_R. An expression for N_R then follows directly.

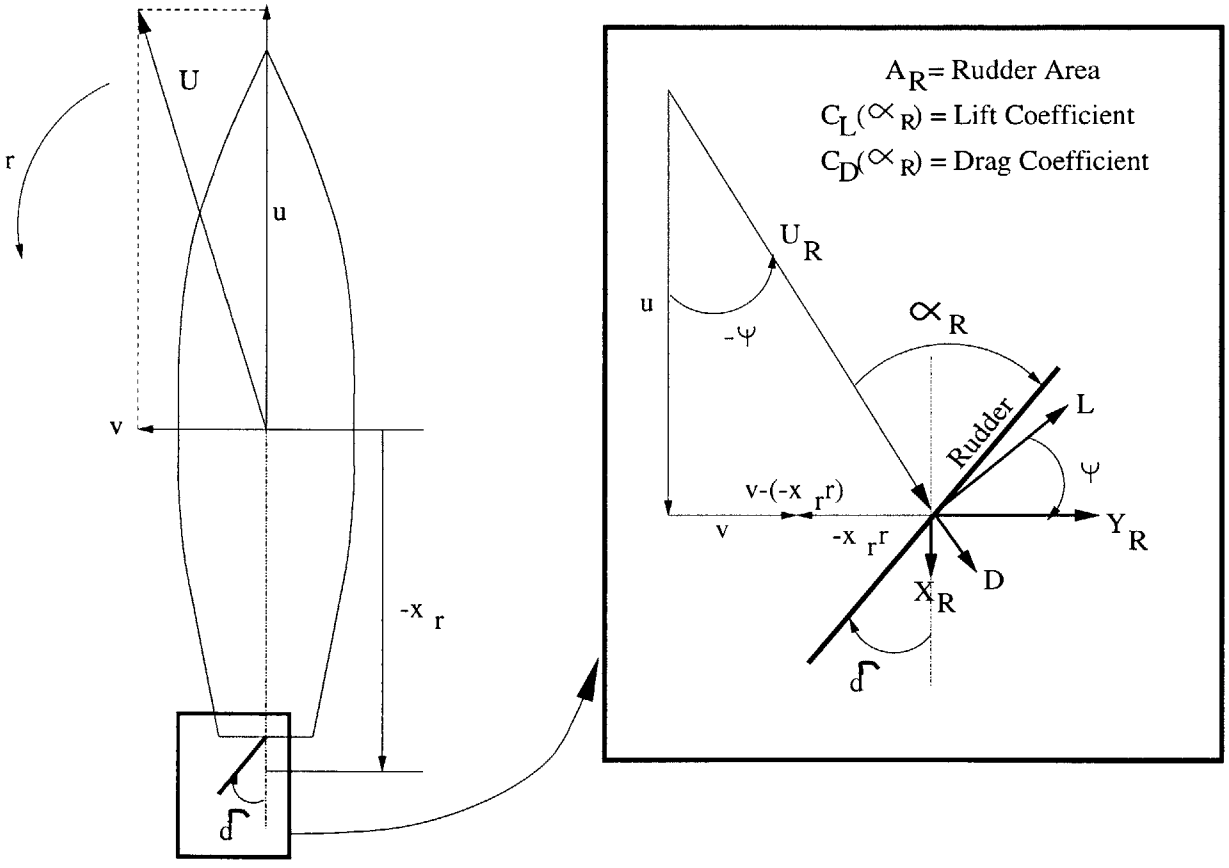

Figure 3-2: Vector Diagram of Rudder Forces

It is well-known that rudders are foils that act as lifting devices when positioned at some angle of attack, α_R, measured with respect to the oncoming flow velocity, U_R. The finite

radius at the leading edge of the foil requires that the lift force, L, act perpendicular to the oncoming flow [49]. Orthogonality of lift and drag requires that the drag force, D, act parallel to the flow. The lift and drag forces are defined in equations 3.25 and 3.26.

$$L = \frac{1}{2}\rho A_R U_R^2 C_L(\alpha_R) \tag{3.25}$$

$$D = \frac{1}{2}\rho A_R U_R^2 C_D(\alpha_R) \tag{3.26}$$

When v and r equal zero, α_R is simply the rudder angle, δ. When the ship experiences sway and yaw motions, however, α_R decreases as shown in Figure 3-2 [3]. The angle ψ represents the decrease in the angle of attack due to sway and yaw. Thus, the instantaneous lift and drag forces depend upon the instantaneous flow velocity, U_R, and instantaneous angle of attack, α_R. The quantities shown in Figure 3-2 are determined from the relations shown in equations 3.27 through 3.29.

$$U_R^2 = u^2 + (v + x_r r)^2 \tag{3.27}$$

$$\alpha_R = \delta + \psi \tag{3.28}$$

$$\psi = \arctan\left(\frac{v + x_r r}{u}\right) \tag{3.29}$$

The lift coefficient, $C_L(\alpha_R)$, and drag coefficient, $C_D(\alpha_R)$, can be approximated with any appropriate model. A typical value for the drag coefficient of a foil is 0.0085 [31]. The lift coefficient can be modeled as a constant for small angles of attack [49]. Use of the modular rudder model allows the use of this approximation even in maneuvers where it appears to be invalid (i.e. a 20^o rudder turn). This is because the actual angle of attack decreases rapidly with respect to the nominal as sway speed and yaw rate increase. Reference [3] used a 20^o rudder turn to validate nonlinear coefficients identified in more violent maneuvers. This can be taken to mean that in that work, this type of maneuver was considered to be at least mildly nonlinear. The sequel will show, however, that this approximation works quite well for maneuvers of this type. For foils with aspect ratio (AR) greater than 1, [49]

[3] Figure 3-2 shows an apparent increase in the angle of attack for illustration purposes only. ψ always opposes δ to allow the forces to balance in steady state.

provides the following expression for the linear lift coefficient, C_L:

$$C_L = \frac{\partial C_L}{\partial \alpha_R} = \left(\frac{1}{0.18\pi} + \frac{1}{\pi AR} + \frac{1}{2\pi (AR)^2} \right)^{-1} \tag{3.30}$$

Thus, taking $C_D = 0.0085$ and computing C_L from equation 3.30, the lift and drag forces may be computed from equations 3.25 through 3.29. Once the lift and drag forces are known, the rudder forces are computed with equations 3.31 through 3.33 where the factor of two accounts for the fact that the ship has two rudders.

$$X_R = 2(L \sin\psi - D \cos\psi) \tag{3.31}$$

$$Y_R = -2(L \cos\psi + D \sin\psi) \tag{3.32}$$

$$N_R = x_r Y_R \tag{3.33}$$

3.2.2.5 Hull/Fluid Interaction Forces and Moments

The forces and moments generated by the interaction between the fluid and the hull are functions of several variables. Thus, X_f, Y_f, and N_f may be described by the following equations:

$$X_f = f_1(u, v, r) \tag{3.34}$$

$$Y_f = f_2(u, v, r) \tag{3.35}$$

$$N_f = f_3(u, v, r) \tag{3.36}$$

The open literature provides many expressions for f_1, f_2, and f_3 along with detailed derivations and underlying assumptions[4]. The derivations and assumptions will not be repeated here with the understanding that all equations presented in the sequel conform to all assumptions described in the references from which they were taken.

The major differences between the proposed models lie in their treatment of the nonlinearities. Abkowitz proposed the most well-known form of the equations outlined in [37]. This model proposes a third-order Taylor series expansion of the fluid forces and moments about some steady-state forward equilibrium speed. Hwang [24] further refined this model based upon full-scale maneuvering trials conducted on a series of large tanker ships [3].

[4]See [2], [3], [7], [13], [26], [52], and [54].

Blanke [5] proposes a simpler form of the equations intended to capture the most important nonlinearities in terms of speed and propulsion loss. The form of the simulation equations chosen for this study is a hybrid of the models proposed in [5] and [24]. It should be noted that each of the models mentioned here are based upon the holistic method described in 3.2.2. Because this work employs the modular method, the hydrodynamic derivatives associated with the rudder forces in these models[5] are captured by the rudder model described in 3.2.2.4. Thus, f_1, f_2, and f_3 are expressed as follows[6]:

$$X_f = f_1(u, v, r) = X_{\dot{u}}\dot{u} + X_P + X_h \tag{3.37}$$

$$Y_f = f_2(u, v, r) = Y_{\dot{v}}\dot{v} + Y_{\dot{r}}\dot{r} + Y_h \tag{3.38}$$

$$N_f = f_3(u, v, r) = N_{\dot{v}}\dot{v} + N_{\dot{r}}\dot{r} + N_h \tag{3.39}$$

Added mass and added inertia terms associated with accelerations (i.e. $\dot{u}$, $\dot{v}$, etc.) can be calculated to within sufficient accuracy for purposes of control systems through hydrodynamic strip theory. The terms X_h, Y_h, and N_h in equations 3.37 through 3.39, however, represent some combination of unknown damping and nonlinear terms whose values no existing hydrodynamic theory can predict with any level of accuracy. These terms are currently determined through extensive model testing. Thus, the linear damping and pertinent nonlinear terms must be estimated to provide at least some knowledge to be beneficial in the design of a control system.

3.3 Nonlinear Simulation Equations of Motion

Completing the steps that follow results in the final form for the nonlinear simulation equations of motion.

1. Apply the simplifications and assumptions discussed in 3.2.2.1 through 3.2.2.3.

2. Introduce the resulting expressions for X, Y, and N to equations 3.9, 3.10, and 3.11.

3. Solve the resulting system of equations for the state derivatives and obtain a system in the state-space form of equation 2.10.

[5] $X_{\delta\delta}$, Y_δ, N_δ, etc.

[6] Equations 3.37 through 3.39 employ standard SNAME notation for hydrodynamic derivatives. Thus, the coefficients in the Taylor series expansion $\frac{1}{2!}$, $\frac{1}{3!}$, etc. are absorbed by the hydrodynamic coefficients. See [37] for details.

The final model which results from completing each of the steps listed above appears in Table 3.2. Coefficients of added mass and added inertia terms in Table 3.2 are determined from valid hydrodynamic theory and knowledge of the ship geometry. Coefficients of the linear damping terms and any nonlinear terms (i.e. components of X_h, Y_h, and N_h) are to be treated as the unknown parameters to be estimated using the SAEKF.

Table 3.2: Nonlinear Simulation Equations

$$\dot{u} = \frac{f_1}{m - X_{\dot{u}}}$$

$$\dot{v} = \frac{(I_z - N_{\dot{r}})f_2 - (mx_g - Y_{\dot{r}})f_3}{f_4}$$

$$\dot{r} = \frac{(m - Y_{\dot{v}})f_3 - (mx_g - N_{\dot{v}})f_2}{f_4}$$

$$\dot{n} = \frac{\eta_r \lambda \eta_g Q_E - Q_P}{2\pi I_p}$$

$$f_1 = \eta_1 n^2 + \eta_2 nu + \eta_3 u^2 + X_h + X_R$$

$$f_2 = Y_h + Y_R$$

$$f_3 = N_h + N_R$$

$$f_4 = (I_z - N_{\dot{r}})(m - Y_{\dot{v}}) - (mx_g - Y_{\dot{r}})(mx_g - N_{\dot{v}})$$

$$\eta_1 = \rho D^4 K_0$$

$$\eta_2 = (1 - w)\rho D^3 K_1$$

$$\eta_3 = (1 - w)^2 \rho D^2 K_2$$

Coefficients of inertial terms such as $Y_{\dot{v}}$ and $N_{\dot{r}}$ to be determined from hydrodynamic theory. Pertinent terms in X_h, Y_h and N_h to be estimated with SAEKF.

Chapter 4

DDG-51 System Identification

Effective control system design relies upon simplified models that adequately describe the dominant dynamics of the plant to be controlled. These simplified models must contain the minimum number of parameters required to sufficiently describe the forces and moments acting on the plant. The equations developed in Chapter 3 are intended to describe the complete nonlinear plant dynamics. The dominant forces and moments are often captured by linear terms over a surprisingly wide range, however. Modern control system theory provides the capability to design controllers that are robust in the face of modeling errors. Thus, the first step in design is to design a controller based upon a linear model and test its performance on the nonlinear plant.

The linear ship dynamics are governed by added mass and added inertia terms, as well as linear damping terms [37]. Hydrodynamic theory provides sufficiently accurate methods for calculating the former. Plant stability, however, is governed by the latter, for which no theory provides sufficiently accurate results. These terms must be determined experimentally. Several experimental methods for determining these terms are outlined in [37]. The drawback to these experimental methods is that they require expensive equipment and labor in addition to a scale model to collect the necessary data. A method of determining these terms using only the scale model is one of the focal points of this study.

4.1 Linear Ship Dynamic Equations

Ships operating at sea most often conduct maneuvers that lie within the linear regime. For example, ships in normal operating conditions do not usually use very large rudder angles

in turns. The most common rudder angles are often between 10-15^o. This type of maneuver lies well within the linear regime. During such maneuvers, forward speed loss and propeller rotational speed loss are small. They do exist, but for the purposes of control system design, they are sufficiently small such that they do not significantly effect the performance of the controller. This implies that the surge equation, $\dot{u}$, and the propeller speed equation, $\dot{n}$, in Table 3.2 are uncoupled from the sway equation, $\dot{v}$, and the yaw equation, $\dot{r}$. Thus, the identification process reduces to the determination of f_2 and f_3.

Table 3.2 shows that f_2 and f_3 each contain two terms which describe the hull damping forces and the rudder forces. The rudder force model developed in 3.2.2.4 is based solely upon wing theory and the kinematics of the problem. Thus, this force is assumed to be accurately modeled and requires no identification. Therefore, the identification problem reduces to determining the hull damping forces, Y_h and N_h. Abkowitz [37] suggests that in the nonlinear case, these terms are adequately modeled with a third order Taylor series expansion. This expansion, however, contains a very large number of terms which is intractable from a control system perspective. For linear maneuvers, however, the expansion may be truncated after the first order terms. This truncation leads to the following expressions for f_2 and f_3:

$$f_2 = -Y_v v - (m - Y_r)r \tag{4.1}$$

$$f_3 = -N_v v - (mxg - N_r)r \tag{4.2}$$

Thus, for the case of linear maneuvers, the identification problem is reduced to the determination of the parameters $-Y_v$, $(m - Y_r)$, $-N_v$, and $(mxg - N_r)$. The negative sign on Y_v and N_v was introduced to maintain the convention outlined in [49] that $-Y_v$ should have a large positive value.

4.2 Initial Identification

The $10^o/10^o$ zig-zag maneuver proposed in [3] was used to determine the linear coefficients. This type of maneuver lies well within the linear regime and also provides "persistence of excitation". Reference [34] states that "An open-loop experiment is informative if the input is persistently exciting." This effectively states that the system dynamics must be

continually excited in order to get any information about the parameters. A steady turn, for instance, would quickly reach a steady state and provide no more dynamic information to update the filter. Thus, persistent excitation is crucial to successful identification.

Recall that the model generating the measurement data was taken from [43]. This model was adapted from a form proposed by Inoue in [26]. The model is parametrically based on full-scale data obtained from experiments performed over a range of operating conditions. The model suffers, however, during a simulated zig-zag maneuver. The implementation of the model in [43] suffers from a drift effect due to the rudder model. Figure 4-1 illustrates this effect.

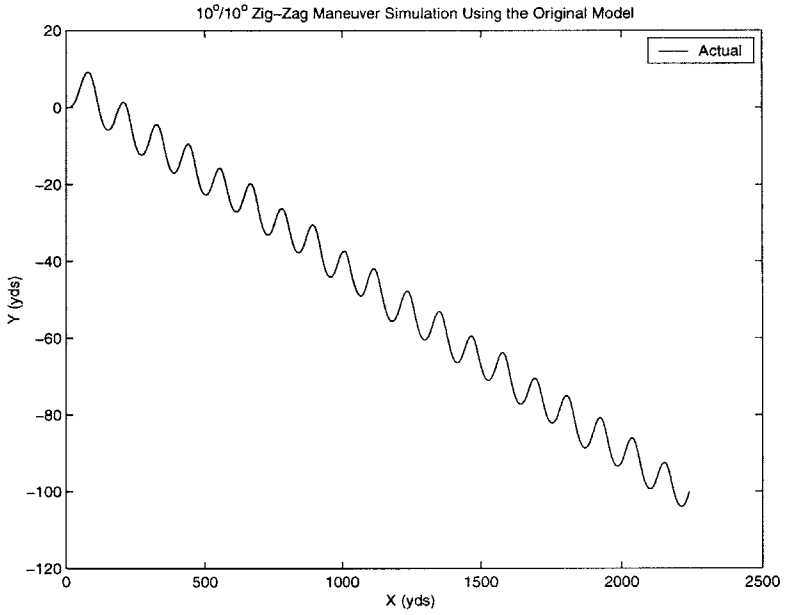

Figure 4-1: $10^o/10^o$ Zig-Zag Maneuver Using the Rudder Model in [43]

Initial attempts at identifying the coefficients using this model produced biased results. Because no a priori information was available for the value of the unknown parameters, the only way to determine success or failure of identification was through simulation. Figures 4-2 and 4-3 show the values obtained through identification and the resulting simulation.

4.2.1 Bias and Divergence in the Extended Kalman Filter

Divergence and bias in the Kalman Filter is well-documented in the open literature. Divergence and bias, however, do not imply filter instability. The EKF possesses some guaranteed

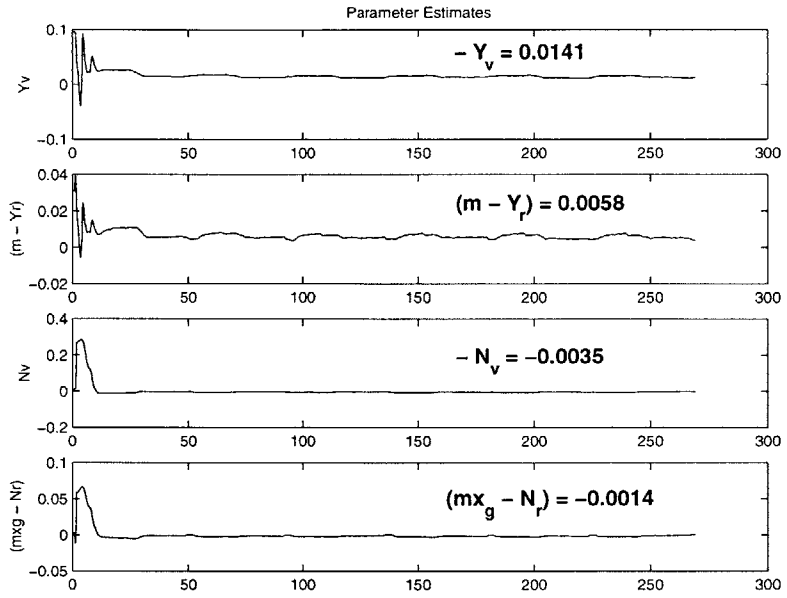

Figure 4-2: Parameter Estimates Using the Rudder Model from [43]

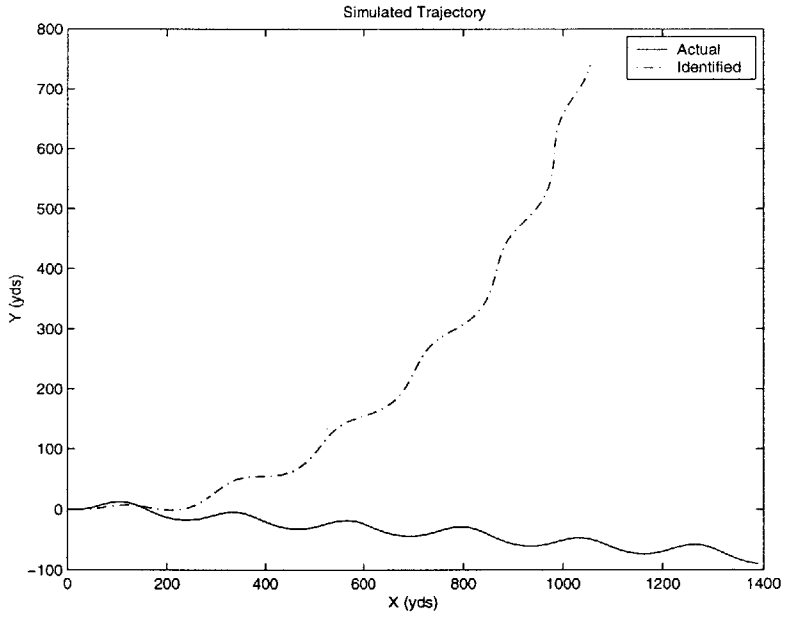

Figure 4-3: Trajectory Simulation Using the Rudder Model from [43]

stability properties under a few mild conditions [20]. Thus, the filter can exhibit "apparent divergence" [12] and give incorrect (biased) parameter estimates. References [12] and [44] propose that bias is caused primarily by errors in the filter model. This suggestion is well-supported by [14] and [30]. Reference [22] provides numerical examples of the effects erroneous models can have on the performance of the filter. Each of these suggest that the model of the plant used in the filter must be sufficiently close to the actual plant to guarantee reliable results.

The process noise covariance matrix, $\mathbf{Q}$, used in the filter model is meant to account for modeling errors. Thus, the choice of $\mathbf{Q}$ represents a critical filter design parameter. If the process noise is chosen too small, the filter "learns" the wrong state values too well. This means that the error covariance decays too rapidly and the filter ignores any additional information contained in the measurements. Thus, the process noise may be said to "drive" the filter and ensure that it does not place undue weighting on its own estimates. Increasing the process noise, however, has a strong effect on the convergence of the filter. Thus, it can not be chosen too high or the filter will not converge. In an effort to account for the bias, identifications were attempted using a wide range of process noise values ranging from 0 and covering two orders of magnitude. Similar results were obtained in all cases.

Much work has gone into developing an analytical method for determining the process noise covariance. Reference [46] proposed a method for handling noise covariances through post-processing of data. References [18], [39], and [40] all propose methods for estimation of the covariances in real-time. Friedland proposes another method for estimating the bias terms in real-time in [14].

4.2.2 Treatment of the Biased Estimates

Favorable application results were demonstrated in each of the works cited above. Application of these techniques to the ship maneuvering problem, however, has not been demonstrated to the author's knowledge. The most favorable application of the SAEKF technique to the ship maneuvering problem is summarized in [3], which is the culmination of 10 years of research conducted at the Massachusetts Institute of Technology (MIT). The details are outlined in the combined works of [6], [21], [24], [35], and [47]. It is evident in [24] that bias was a problem as well, although it is not explicitly described. In that work, the assumed form of the simulation model was significantly altered from the Taylor expansion

form proposed in [2] and [37] to obtain favorable results.

This rationale has been adopted in this work as well. The drift illustrated in Figure 4-3 most likely results from numerical problems in the model from [43] due to its parametric nature. The linear dynamics of ship maneuvering are well-documented and the assumed form shown in equations 4.1 and 4.2 are not likely to be overly erroneous. For these reasons, the rudder model used in [43] was replaced with the rudder model derived in 3.2.2.4. Any further references to this model assume this modification has been made.

4.3 Identification of the Linear Damping Coefficients

4.3.1 Noise Parameters

The magnitude of the process noise covariance matrix, $\mathbf{Q}$, and the sensor noise covariance matrix, $\mathbf{R}$, determine the weighting the filter applies to its own estimates and the measurements, respectively. During the course of the study, the trade-off between the two became evident. Given the sophistication of current digital modern measurement devices, the non-dimensional measurement noise was chosen in all cases as $\mathbf{R} = 0.01\mathbf{I}$[1]. When the process noise is too small, the filter"trusts" its own estimates too much and, thus, gives a very low weighting to the measurements (i.e. low gains). This introduces the bias discussed in 4.2.1. Figures 4-4 and 4-5 illustrate this phenomenon.

The identification uses the nonlinear model from [43] to generate the data and the filter employs the linear model described in 4.1. Figure 4-4 shows that the states are apparently tracked quite closely. Note, however, that the filter never updates the surge speed, u. This is caused by the fact that the absence of process noise implies perfect modeling of the plant dynamics. Therefore, the filter has no reason to update its own propagated estimates (i.e. low gains). The close tracking of the sway speed, v, and the yaw rate, r, indicate that the nonlinear terms in these equations contribute very little during a linear maneuver. This indicates that the dynamics are modeled with sufficient accuracy. Thus, the filter is justified in trusting its own propagated estimates.

Figure 4-5 shows the parameter estimates during the identification. Note how each of the parameters converges nicely to a constant value. This indicates that the error covariance

[1]This value is of the same order of magnitude as the non-dimensional forces, which is believed to be conservative.

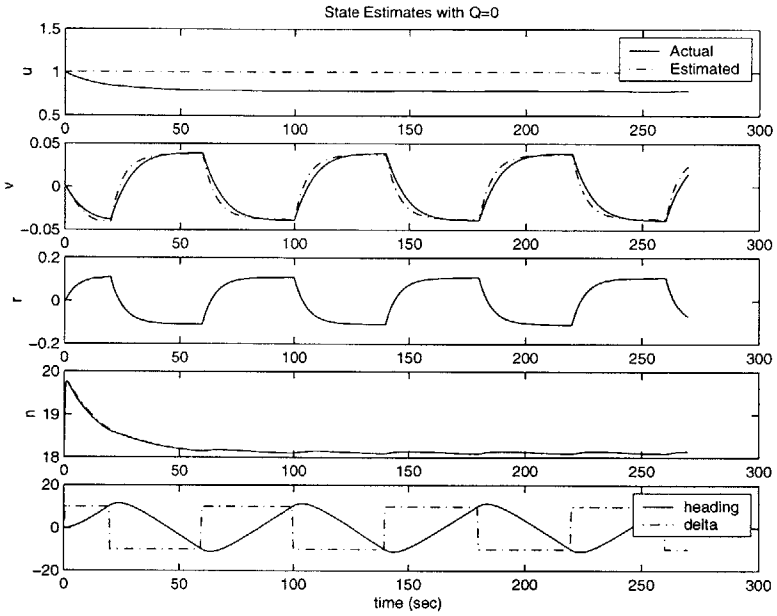

Figure 4-4: State Estimates During a $10^o/10^o$ Zig-Zag Maneuver with Q=0

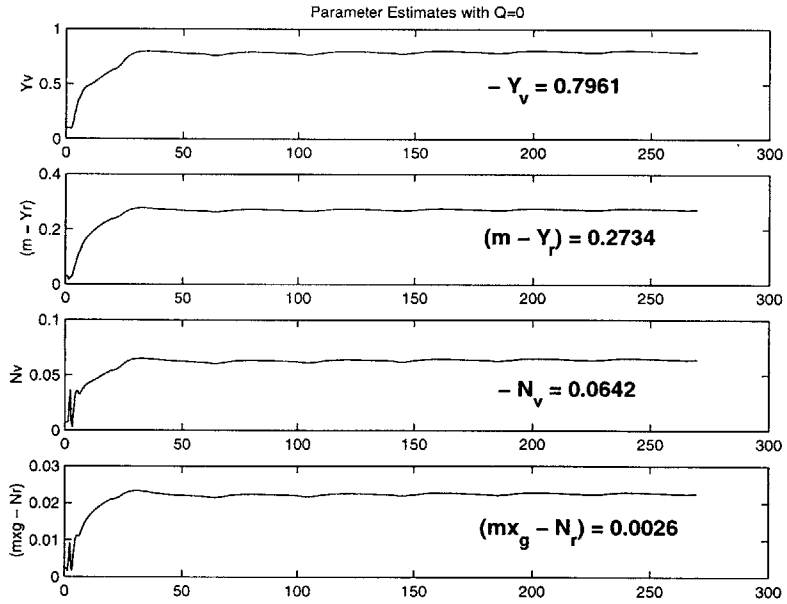

Figure 4-5: Parameter Estimates During a $10^o/10^o$ Zig-Zag Maneuver with Q=0

has decayed to zero and the filter stops updating the estimates. Recall the expression for the gains, $\mathbf{K_k}$, from Table 2.1. This equation implies the following:

$$\mathbf{K_k} \rightarrow 0 \text{ as } \mathbf{P_k}(-) \rightarrow 0 \Rightarrow \underline{\hat{x}}_k(+) = \underline{\hat{x}}_k(-) \tag{4.3}$$

The results in Figure 4-5 are misleading, however, since they exhibit apparent divergence [12]. Figure 4-6 illustrates the results of the simulation after identification. The steady turn is chosen as the simulation maneuver to illustrate the performance of the filter estimates in a maneuver other than that used to identify the coefficients. Figure 4-6 shows that, while

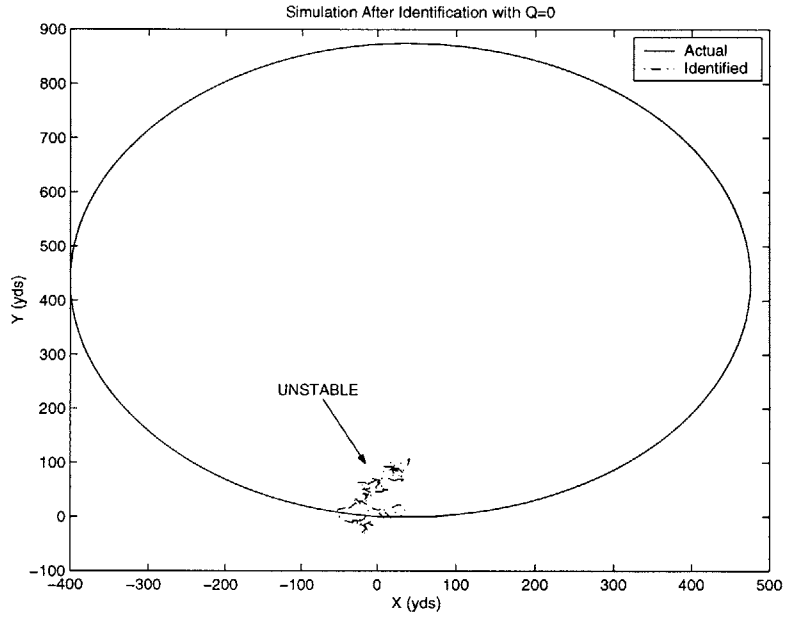

Figure 4-6: Simulation of a 10^o Rudder Steady Turn with Q=0

the filter does converge, the estimates produce an unstable plant.

If perfect modeling of the system dynamics were possible, and the estimates still proved to be biased, the designer may introduce some "fake" noise into the system. This "fake" noise would continue to drive the parameters once the state estimates have converged and cause the filter to weight the measurements more heavily. This technique is outlined in [18] and suggests that a value of 0.1% of the nominal parameter value is suitable for this purpose. This approach fails, however, for two reasons. First, using a "nominal" parameter value implies some a priori knowledge of the plant. In this case, as in most cases in the physical world, this does not exist. Second, because the non-dimensional parameter values are small,

once the state estimates have converged the weighting on the measurements will be very small as well. Thus, the small weighting on the measurements tends to drive the filter very slowly. Thus, it will not converge in any reasonable period of time. Figure 4-7 illustrates the effect of the "fake" noise. Note how the parameters appear to be slowly decaying with time. The slope is so gradual, however, that the filter will require an unacceptable amount of time to converge (if it does at all).

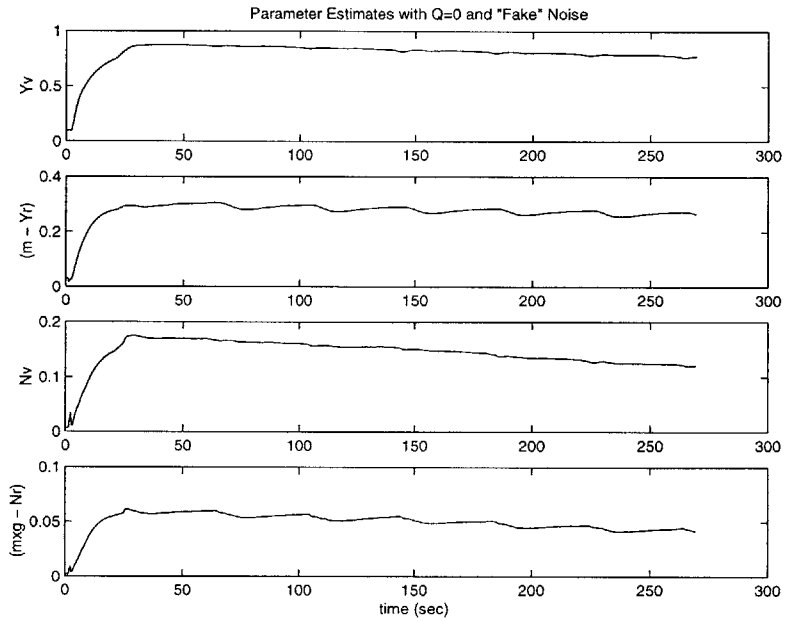

Figure 4-7: Parameter Estimates

Given the previous considerations, the appropriate noise parameters must consist of some combination of process noise and "fake" noise such that the filter continues to utilize the information contained in the measurements. The appropriate combination of these noise parameters was chosen through an iterative process of identification and simulation. Large process noise was required to effectively track the states. This large process noise, however, caused rapid convergence to the true state values. Thus, "fake" noise was also required to continue to drive the parameters to their true values. The combination of the two noise parameters allowed the filter to update its dynamical model, as well as obtain information from the measurements until a balance was achieved. The measurement noise was chosen as described in 4.3.1. The final values of the noise parameters are listed in Table 4.1.

Table 4.1: Identfication Noise Parameters

Process Noise Driving the State Estimates, Q	0.05
Fake Noise Driving the Parameter Estimates, FQ	0.01
Measurement Noise, R	0.01

4.3.2 Physical State Estimation

The identification process was again conducted using the $10^o/10^o$ zig-zag maneuver. The filter model was linear with $\dot{u} = \dot{n} = 0$ and the measurement data was generated with the full nonlinear model from [43]. The noise parameters were those listed in Table 4.1. The results of the identification of the physical states are illustrated in Figure 4-8.

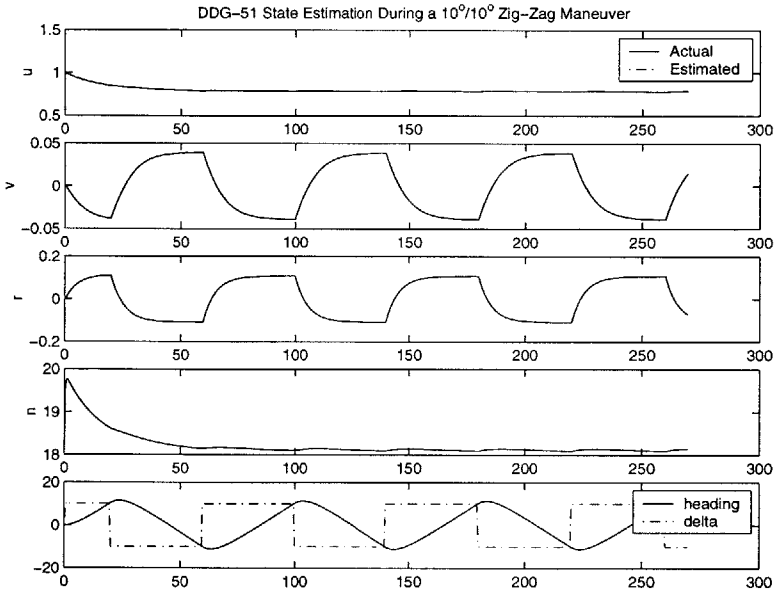

Figure 4-8: State Estimates During a $10^o/10^o$ Zig-Zag Maneuver

Figure 4-8 illustrates the filter's ability to track the physical states despite the inadequate modeling of the dynamics of surge speed, u, and propeller revolutions, n. This is because the process noise is large enough to account for the errors in the dynamic model. The process noise in the system causes the filter to weight the measurements more heavily than the estimates (i.e. large gains) due to the uncertainty in the dynamic model of the plant. Because the measurement noise is considerably smaller than the process noise, and the surge speed and propeller revolutions are measured quantities, the filter tracks them quite

well. The filter also does an excellent job of tracking the sway speed, v, and yaw rate, r. This, again, is due to the fact that sway and yaw are measured quantities and the process noise is high. Further, because the nonlinear effects are small in this type of maneuver, the dynamic model for these two terms is quite accurate.

4.3.3 Parameter Identification

The four additional states in the filter represent the unknown parameters to be estimated. Previous sections demonstrated the filter's ability to track the physical states closely, while giving inaccurate (biased) parameter estimates due to modeling errors and erroneous assumptions in the noise statistics. The iterative process of identification and simulation produced the parameter estimates illustrated in Figure 4-9.

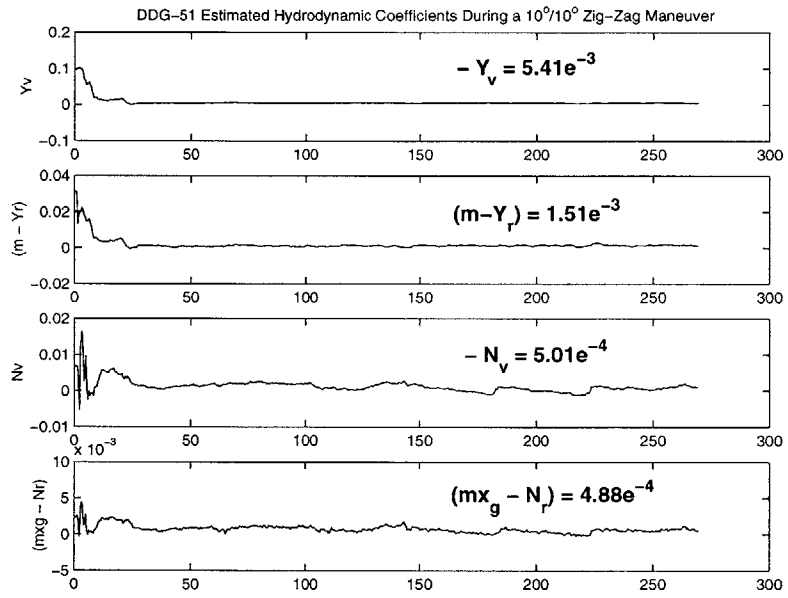

Figure 4-9: Parameter Estimates During a $10^o/10^o$ Zig-Zag Maneuver

With the exception of Y_v, the parameter estimates exhibit variations about some value. This could prove to be problematic if the goal of the identification were to establish exact coefficient values. The goal of control system design is to develop controllers that perform well with only an approximate knowledge of the coefficients. In fact, parameters that model the state values within 40% of the actual values often leads to acceptable control system performance. Fortunately, this goal is often achieved. Thus, to determine the coefficient value to be used in the simulation, the mean value of the last 67% of the parameter estimates

was taken to be the parameter value.

4.3.4 DDG-51 Simulation After Identification

The ultimate goal of an automatic maneuvering control system on a ship is to provide a reliable method of maintaining a desired trajectory. Linear control system theory has been proven to be quite reliable in designing control systems for plants in which nonlinearities are weak. Control of an inverted pendulum represents an excellent example of this assertion [2]. Because ship maneuvers normally lie within the linear regime, where nonlinear effects are small, a control system design based upon a linear ship model could very likely perform quite well. Figures 4-10 and 4-11 illustrate the simulation results using the identified parameter values.

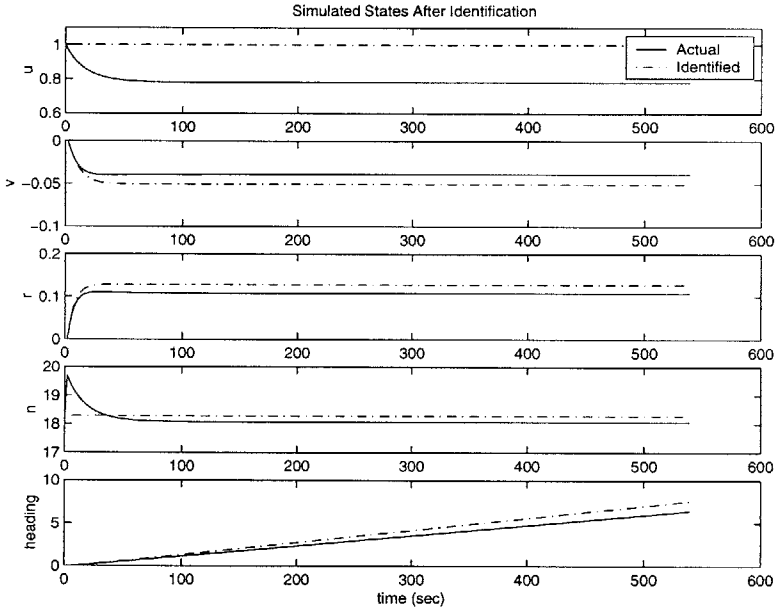

Figure 4-10: Simulated States During a 10^o Rudder Steady Turn

Figure 4-10 shows that the identified model tracks the actual nonlinear model quite closely in sway and yaw. It does not, however, track surge and propeller revolutions at all. This is because the simulation model ignores forward speed loss and propeller speed loss (i.e. $\dot{u} = \dot{n} = 0$). This is a good assumption because the actual speed loss in the simulation is about 20% and propeller speed loss is approximately 10%. These represent ideal errors for the application of linear theory to a nonlinear physical system. The lack of speed loss

[2]See example 2.1-1 in [33].

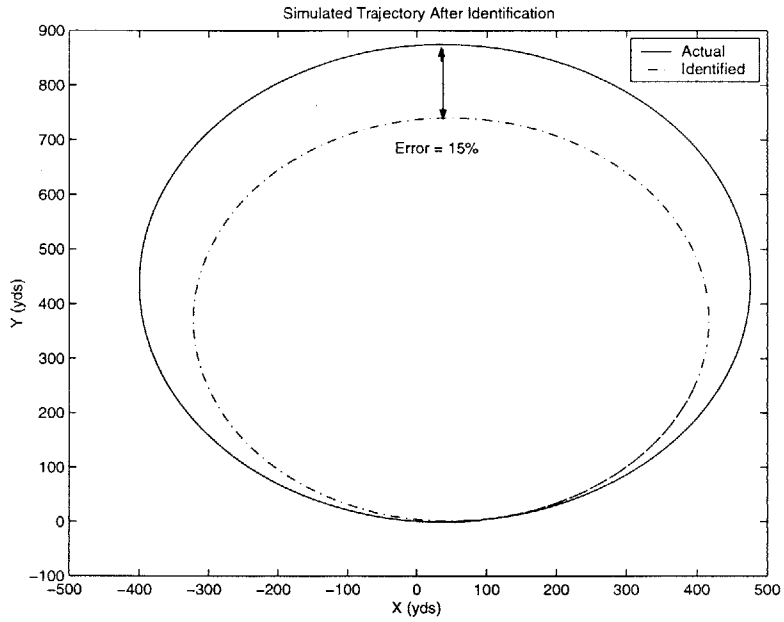

Figure 4-11: Simulated Trajectory During a 10^o Rudder Steady Turn

accounts for the higher values of sway and yaw. Higher speed in a turn implies a tighter turn, and thus, higher values of sway and yaw.

Figure 4-11 shows the trajectory produced by the identified model. The error in the turning diameter between the identified and actual models is approximately 15%. This situation is ideal for the application of linear control theory to develop automatic controllers for the ship. Note that the identified model has a tighter turning diameter than the actual model. This was expected due to the higher values of sway and yaw shown in Figure 4-10. The identified model maintains higher speed throughout the turn. Thus, it has a smaller turning diameter.

Chapter 5

Controller Design

The previous chapters focused on the identification of the linear damping terms in the DDG-51 equations of motion. The identification process resulted in determination of the hydrodynamic coefficients that produce the dominant forces and moments during linear ship maneuvers. Thus, these terms may be employed to develop simple models which may form the basis for simple course-keeping controllers.

The sequel describes the design of two controllers based upon simplified ship models. The first controller is a heading autopilot. The second controller regulates the lateral deviation (cross-track error) from the desired reference trajectory. The desired frequency responses are developed using a loopshaping technique. The desired control laws are then determined from the design loopshape. Simulations are then performed on the nonlinear ship model using the linear controllers to evaluate their performance.

5.1 Controller Design via Loopshaping

Controller design via loopshaping is well-documented in many texts on feedback and optimal control system design. More detailed versions of the following presentation are described in [11], [33], and [53].

The overall goal of controller design via loopshaping is illustrated in Figure 5-1. The *Loop Gain* should be designed such that the closed-loop plant exhibits *robust performance* [11]. This means that the entire system (plant and controller) exhibit good performance and tracking at low frequencies within the system *bandwidth*. The system must also be robust to high-frequency disturbances such as sensor noise and unmodeled dynamics. The

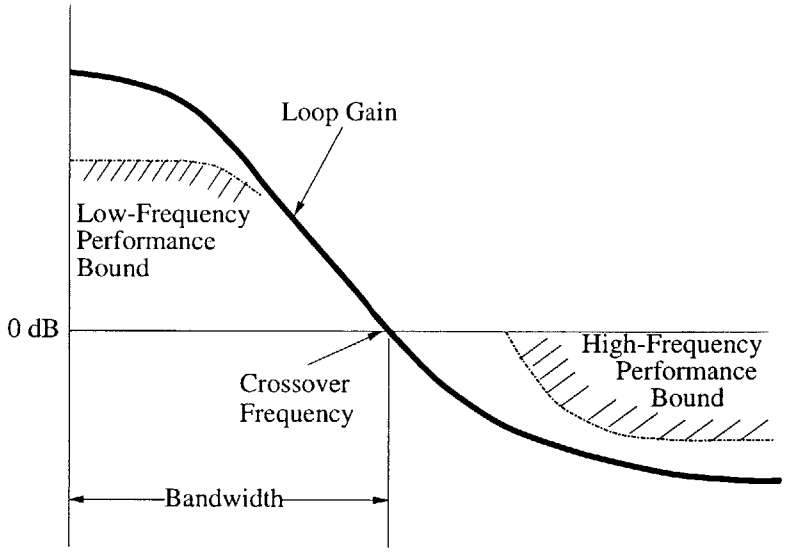

Figure 5-1: The Goal of Loopshaping

sequel describes how this process is accomplished by the control system engineer.

5.1.1 Feedback Control

Figure 5-2 represents a typical feedback control system with the plant disturbance input, d, reflected to the plant output as in [33]. Reference [11] considers the feedback loop with the disturbance reflected at the plant input. The derivation of [33], however, makes the effect of the disturbance and desired properties of the loopshape a bit more clear. Thus, it is primarily that derivation that will be presented here.

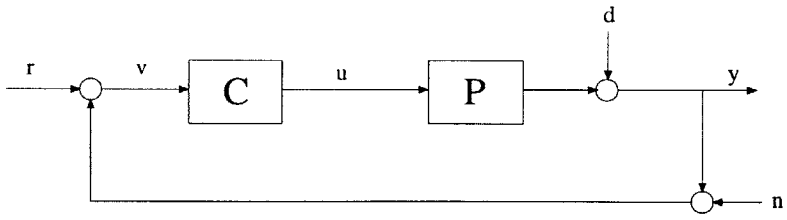

Figure 5-2: Typical Feedback Loop

The goal of a feedback control system is for the plant output, y, to asymptotically track a desired reference output, r. The plant, P, however, is acted upon by disturbances, d, which represent external disturbances and modeling errors. Further, the measurements of the output are influenced by sensor noise, n. The goal of the controller, C, is to compute

the control input, u, that regulates the output and maintains the desired reference value despite the disturbances and measurement noise. Defining the tracking error, e, as follows,

$$e = r - y \tag{5.1}$$

examination of Figure 5-2 gives rise to the following expressions:

$$v = r - y - n \tag{5.2}$$

$$y = PCv + d \tag{5.3}$$

5.1.2 System Sensitivity, Cosensitivity, and Loop Gain

To illustrate the ideas behind loopshaping theory, one requires expressions for the closed-loop transfer function relations of the desired outputs, y and e, to the deterministic and stochastic inputs, r, d, and n respectively. Substituting equation 5.2 into equation 5.3 results in the following expression for y

$$y = PC(r - y - n) + d \tag{5.4}$$

$$(I + PC)y = PC(r - n) + d \tag{5.5}$$

$$y = (I + PC)^{-1}PC(r - n) + (I + PC)^{-1}d \tag{5.6}$$

$$y = PC(I + PC)^{-1}(r - n) + (I + PC)^{-1}d \tag{5.7}$$

where the final operation is justified because PC is square and invertible [33]. The expression for the error, e, may be derived in a similar manner.

$$e = r - PCv - d \tag{5.8}$$

$$e = r - PC(r - y - n) - d \tag{5.9}$$

$$e = r - d - PC(e - n) \tag{5.10}$$

$$(I + PC)e = r - d + PCn \tag{5.11}$$

$$e = (I + PC)^{-1}(r - d) + (I + PC)^{-1}PCn \tag{5.12}$$

$$e = (I + PC)^{-1}(r - d) + PC(I + PC)^{-1}n \tag{5.13}$$

Equations 5.14, 5.15, and 5.16 define the *system sensitivity*, S, *cosensitivity*, T, and *loop*

gain, L, respectively.

$$S = (I + PC)^{-1} \tag{5.14}$$

$$T = PC(I + PC)^{-1} \tag{5.15}$$

$$L = PC \tag{5.16}$$

Notice that $S+T = I$. Thus, S and T may not both be made arbitrarily large. Substituting equations 5.14 and 5.15 into equations 5.7 and 5.13 results in the following expressions for the output, y, and the tracking error, e:

$$y = T(r - n) + Sd \tag{5.17}$$

$$e = S(r - d) + Tn \tag{5.18}$$

System disturbances are low-frequency phenomena such as wind and wave forces exerted on the ship hull. Examples of high-frequency phenomena are sensor noise and structural vibrational modes. The goal of the controller is to respond to low-frequency disturbances within the bandwidth of the system and attenuate disturbances outside the system bandwidth where its behavior is not as well-known. For example, the controller should respond to wave disturbances to maintain the desired output, but should not respond to high-frequency structural vibrational modes whose dynamics were neglected in the system model.

At low frequencies, equations 5.17 and 5.18 may be expressed as follows:

$$y \approx Tr + Sd \tag{5.19}$$

$$e \approx S(r - d) \tag{5.20}$$

At high frequencies the same equations may be represented as follows:

$$y \approx -Tn \tag{5.21}$$

$$e \approx Tn \tag{5.22}$$

because the reference signal is typically a constant or at least slowly-varying. Thus, the *system sensitivity*, S, should be small at low frequencies where the disturbances, d, are significant to ensure small tracking errors. Additionally, if S is small, $T \approx 1$ at low frequencies

(because $S + T = 1$) such that $y \approx r$. Conversely, the *system cosensitivity*, T, should be small at high frequencies where sensor noise and other high-frequency phenomena are significant. If these conditions are satisfied, the controller will exhibit *robust performance* [11]. This implies that the controller provides good tracking of reference inputs (performance) while simultaneously rejecting high-frequency signals where the plant model is not so well understood (robustness).

5.1.3 Performance Specifications

Frequency-dependent weighting functions are required to establish the low and high frequency performance bounds shown in Figure 5-1. These functions establish the minimum and maximum open-loop system gains over all frequencies. Thus, one weighting function should be large (i.e. large positive gains) at low frequencies to ensure good performance. The other weighting function should be small (i.e. negative gains) at high frequencies to ensure robustness.

Determination of these weighting functions, coupled with design of the loop gain, L, then allows development of frequency-domain performance specifications. The idea behind performance specifications may be illustrated on a Nyquist plot [11] as in Figure 5-3. For

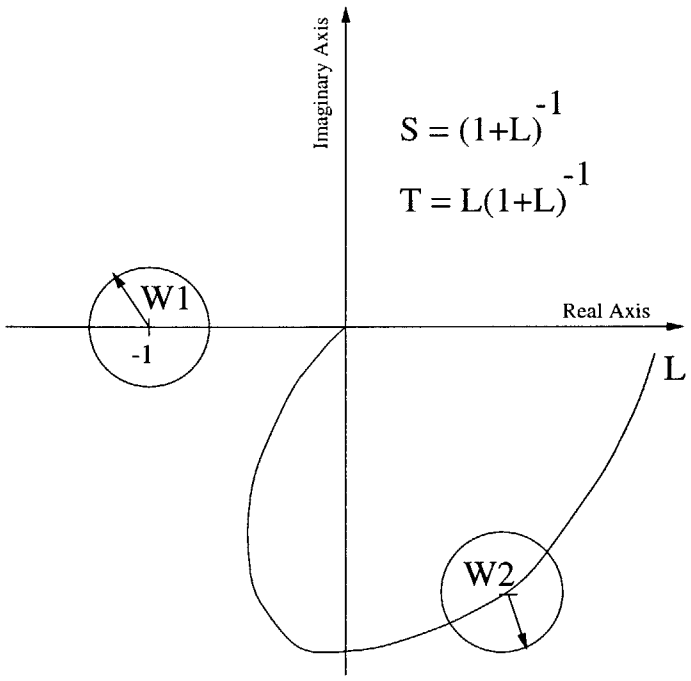

Figure 5-3: Nyquist Plot of Performance Specifications

good tracking, the loci of L must lie outside the disk of radius $W1$ over all frequencies. To ensure robustness in the face of multiplicative plant uncertainties, the disk of radius $W2$ must not pass through the point $-1 + 0j$ over all frequencies.

The goal of the controller is robust performance which implies good tracking and disturbance rejection at low frequencies and attenuation of high-frequency signals such as sensor noise and modeling errors. Recall that the system sensitivity function, S, should be small at low frequencies to provide good performance and the system cosensitivity function, T, should be small at high frequencies to provide robustness. Considering Figure 5-3 and the definitions of the quantities derived previously, it can be shown [11] that the frequency-domain performance specification that ensures robust performance is given by the following expression:

$$\left\| |W_1 S| + |W_2 T| \right\|_\infty < 1 \; \forall \; \omega \tag{5.23}$$

5.1.4 Design Criteria

The length between perpendiculars (LBP) for the DDG-51 class ships is 466 feet. The main low-frequency phenomena in the open sea that influence the ship motions consist of waves and current. Currents are most often constant or at least very slowly varying. Thus, waves represent the phenomena that regularly contain a frequency component.

The frequency of open-ocean gravity waves is related to their characteristic wavelength. The motion of the ship is also related to this wavelength. According to [49], the closed-loop system should respond to wavelengths of the same order as the ship LBP. Thus, the closed-loop system should respond to all wave disturbances of length 400 feet or greater. This corresponds to a characteristic circular frequency of 0.7 radians/second (Period $\approx$ 9 seconds). To allow for some flexibility in the loopshaping, the design crossover frequency, ω_c, should lie in the range between 0.5 - 1.5 radians/sec.

Currents tend to "blow" the ship off course in the same way that wind blows an airplane off its intended course. If this disturbance is not accounted for, the ship would move far from its intended track. Thus, the ship must adjust its heading angle such that it accounts for the drift effect due to the current. Because currents are very low frequency disturbances, the closed-loop system must track them very accurately. Thus, the closed-loop system should track disturbances with an error, β, less than 1% at frequencies below 0.01 radians/sec.

This corresponds to open-loop system gains of at least 40 dB below 0.01 radians/sec. Thus, the open-loop system gains should lie above the low-frequency performance bounds and below the high-frequency performance bounds illustrated in Figure 5-1 while achieving a reasonable closed-loop step response. The ultimate test of any controller design is how it operates on the actual rather than the nominal plant. The reasons for not specifying time domain performance criteria will be addressed in the sequel.

5.2 Autopilot Design

The goal of a ship autopilot is to maintain the ship's actual heading around some slowly-varying reference heading. The autopilot must perform this function in the presence of disturbances, sensor noise, and modeling errors described in 5.1. The design speed for all simulations is 22 knots. This corresponds to the maximum ship speed in a plant configuration with two of the four main engines on-line, one driving each shaft (split plant). Non-dimensionalization of the equations, however, allows this speed to be adjusted without affecting the results. The split plant configuration is required, however, to validate the assumption in Chapter 3 that the steady-state forces and moments due to the propeller cancel.

5.2.1 Dynamic Model

Low frequency ship motions may be described by a first-order model attributed to Nomoto [13]. This model may be represented as follows:

$$T\ddot{\psi} + \dot{\psi} = K\delta \tag{5.24}$$

where ψ represents the ship heading angle and δ represents the rudder angle. Note that the sway dynamics have been removed from the equation of motion. T and K represent the ship time constant and gain, respectively. These terms may be determined from the hydrodynamic coefficients identified in Chapter 4 using the procedures outlined in section

5.3.2 of [13]. This leads to the following values for T and K:

$$T = 1.9287 \tag{5.25}$$

$$K = 2.04 \tag{5.26}$$

Thus, the plant transfer function, P_{ol} from input, δ, to output, ψ, appears in equation 5.27 and represents the change in heading angle to a change in the rudder angle.

$$P_{ol} = \frac{\psi}{\delta} = \frac{K}{s(Ts+1)} \tag{5.27}$$

The ship's rudder contains its own dynamics. For instance, the rudder does not instantaneously change its angle when commanded by the helmsman. According to [24], the rudder dynamics do not play a major role in the identification process because they are much faster than the ship dynamics. For control purposes, however, the rudder dynamics do play a role. Classification restrictions prevent the disclosure of the actual DDG-51 rudder swing rate. Thus, it was assumed in this work that the rudder dynamics could be modeled by the following transfer function, P_{sg}, that maps the commanded rudder angle to the actual rudder angle:

$$P_{sg} = \frac{\delta}{\delta_c} = \frac{6}{s+6} \tag{5.28}$$

Thus, the new plant, P, may be represented as follows:

$$P = P_{ol}P_{sg} \tag{5.29}$$

This new plant, P, corresponds to the plant block in Figure 5-2. To guard against unreasonably large rudder angle commands during maneuvers, a rudder command angle limiter was added to the model as well. This limits the maximum allowable commanded rudder angle during maneuvers to 30^o. This guards against the actual rudder angle approaching the physical stops on the actual ship. The goal now is to design the controller, C, using loopshaping to achieve robust performance.

5.2.2 Loopshaping Controller Design

In some instances, it is possible to shape the loop gain, L, to obtain the desired frequency response. The controller may then be determined as follows:

$$C = \frac{L}{P} \tag{5.30}$$

In other cases, the controller must be designed directly to obtain the desired response. The autopilot design followed the former procedure. The open-loop plant, P, is straight-line stable [37] as are many ships. Thus, the controller is not required to stabilize the plant.

To give this a physical representation, imagine the ship without any control encounters a current. The current will cause an initial yaw rate, but the large wetted surface area in the stern will develop forces and moments that counteract the initial rate of yaw. Thus, the yaw rate will decay back to zero after a finite period. Because the heading angle is simply integral of the yaw rate, or

$$\dot{\psi} = r \tag{5.31}$$

the ship will turn to a heading that faces the current and stay on that heading when $r = 0$. Thus, the goal of the autopilot must be to ensure that the ship continues on its desired heading despite the current.

Thus, the loop gain for the autopilot design may be modeled simply as a second-order system with an integrator whose transfer function may be represented as follows:

$$L = PC = \frac{\omega_n^2}{s(s^2 + 2\zeta\omega_n + \omega_n^2)} \tag{5.32}$$

$$\omega_n = \sqrt{60} \tag{5.33}$$

$$\zeta = 2 \tag{5.34}$$

Figure 5-4 illustrates the results of the loopshaping design. The loopshape has gains of at least 40 dB at frequencies below 0.01 radians/sec. It lies above the low-frequency performance bound indicated by W_1. This indicates good tracking and disturbance rejection at low frequencies. The loop gains roll off at high frequencies indicating good attenuation of high-frequency signals and unmodeled fast dynamics. They further lie below the

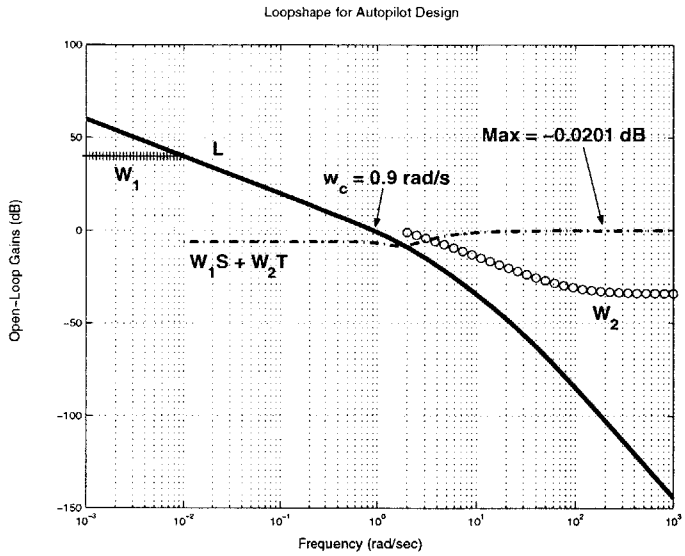

Figure 5-4: Loopshape for Autopilot Design

high-frequency performance bound indicated by W_2. The design also satisfies the robust performance requirement given by equation 5.23.

An indication of overall plant stability may be obtained from the Bode plot. Figure 5-5 indicates a gain margin of approximately 30 dB and a phase margin of approximately 64^o. Reference [49] indicates that a good rule of thumb for gain and phase margins are 3 dB and 30^o, respectively. Thus, the autopilot design falls well within the acceptable range.

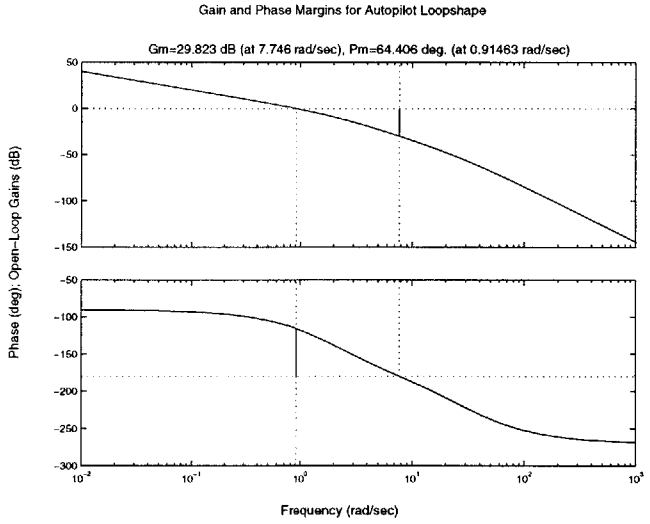

Figure 5-5: Gain and Phase Margins for Autopilot Design

The frequency response of a controller is not its only measure of suitability to the task. The designer must also check the time domain response to ensure adequate closed-loop performance. Reference [36] indicates that acceptable performance for an autopilot is met by the following conditions:

1. No more than 5% overshoot to a step input.

2. 2% settling time less than 5 ship lengths at design speed.

Figure 5-6 indicates that the autopilot design meets these criteria. Additionally, the tracking error at steady-state is less than 1% as dictated by the frequency response.

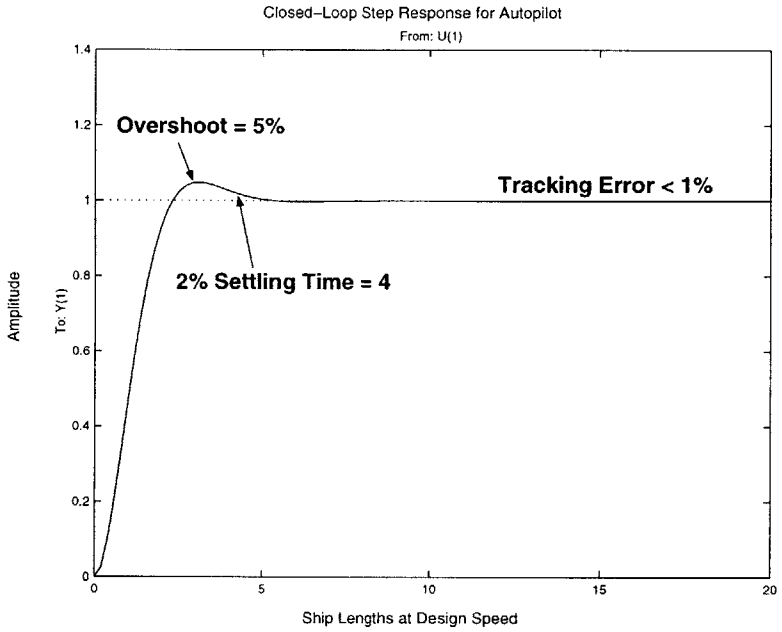

Figure 5-6: Closed-Loop Autopilot Step Response

5.2.3 Closed-Loop Simulations of the Autopilot Design

The true test of a linear controller is how well it performs in conjunction with the nonlinear plant from which it was derived. Incorrect assumptions on the level of uncertainty in the model may lead to poor performance if the unmodeled dynamics have a strong effect on the plant. In this case, this would arise if the nonlinearities in the equations of motion have a strong impact on the dynamics. These nonlinearities are believed to be weak in the ship maneuvering problem, however, as described in Chapter 4. This proved to be true in this study as well.

To validate the controller performance, two different simulations were developed. The first is a simulation of the controller's ability to reject a constant current disturbance equal to 5 knots. For the second simulation, a maneuver was generated by computing the required instantaneous heading angle required for the ship to begin on a steady course and speed and execute a 90^o left turn and steady up on the new heading. After a period of steady operation, the ship then executes a 90^o right turn and steadies up on its new heading.

5.2.3.1 Current Rejection Simulation

Figure 5-7 illustrates the ship's actual trajectory in relation to the dead-reckoned trajectory in the absence of any disturbance. The current in this case must be simulated as an initial condition on the ship's sway velocity, v, due to the fact that the dynamics of position, y, were neglected. The figure shows that the ship gets "blown" approximately 1/3 of a ship

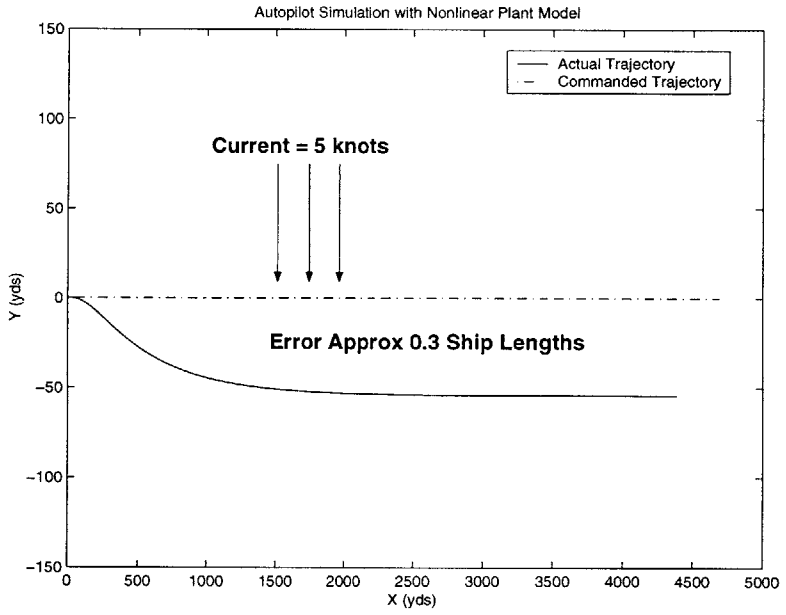

Figure 5-7: Nonlinear Plant Trajectory During Current Rejection

length off its initial track as a result of the current disturbance. It does, however, return to its commanded heading angle [1]. Thus, the controller takes the required action to return the ship to its intended heading.

[1]It should be noted that the standard compass rose has been rotated 90^o in each of the simulations to follow. Thus, a heading of 000 in the figures corresponds to a heading of 090 on a standard compass rose.

Figure 5-8 illustrates the change in ship heading. The ship is initially turned to the right due to the side forces and moments generated by the current interaction with the ship hull. The controller detects the difference between the actual and commanded headings via noisy measurements and generates commands to the rudder to turn the ship to the left and return it to its intended heading. The heading angle in the figure appears to be zero. This is not actually the case, however. The ship actually develops a constant sway velocity that results in a side-slip angle. Thus, while the figure shows the ship's actual heading equal to zero, the ship is actually turned at a small angle into the oncoming current to account for it. Simulations that show the actual heading angle appear in the following section where the dynamics of y are included in the simulation.

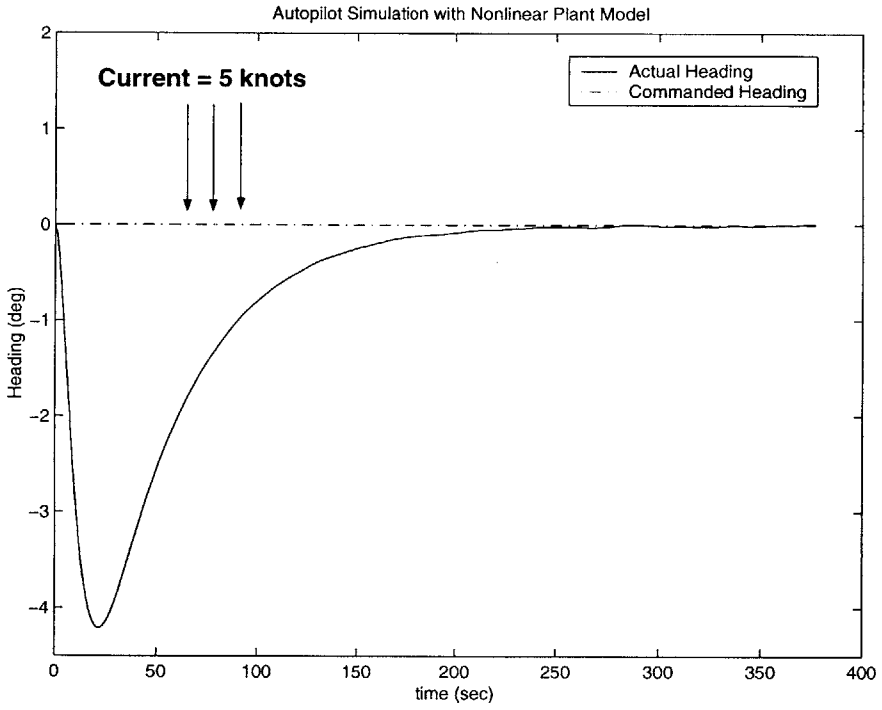

Figure 5-8: Nonlinear Plant Heading Change During Current Rejection

Figure 5-9 demonstrates the commanded and actual rudder angles during the current rejection simulation. The commanded rudder angles may seem excessive at first glance. The figure shows, however, that during the maneuver, inclusion of the rudder dynamics in the equations of motion rejects these high-frequency oscillations. Thus, the actual rudder motion is smooth during the correction. After reaching steady-state, the rudder does exhibit some high-frequency oscillatory motion. The amplitude of these oscillations, however, is less than 0.1^o over periods of several seconds. This is not deemed to be a severe condition that would tend to cause excessive wear on the mechanical components.

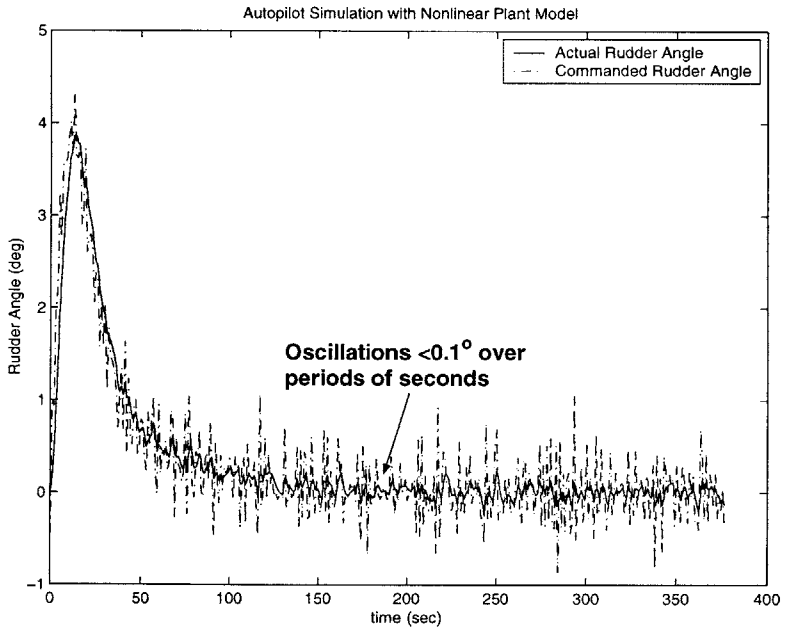

Figure 5-9: Actual and Commanded Rudder Angle During Current Rejection

The reason for these high-frequency oscillations in the commanded rudder angle is illustrated in Figure 5-10. Recall that the goal of loopshaping controller design is to ensure that the closed-loop *combination* of the plant and controller attenuate high-frequency signals. Because the plant has very small gains at high frequencies, the controller is free to have rather large gains at these frequencies. Thus, because the input to the controller is the noisy, high-frequency measurement of the heading angle, the controller responds in kind. The controller gain at the measurement frequency is approximately 8 dB. Thus, the controller actually amplifies the measurement noise. The plant gain, however, at the same frequency is approximately -33 dB. Thus, the effect of the noise on the entire closed-loop

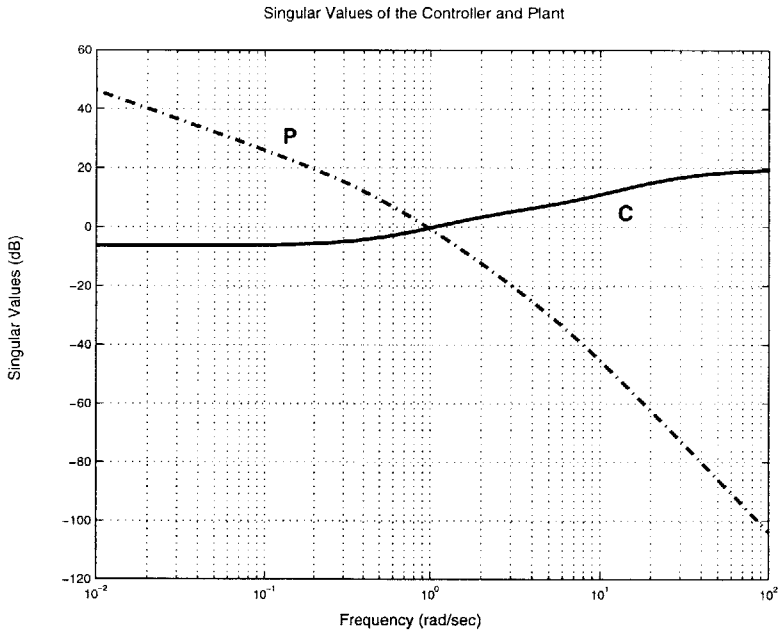

Figure 5-10: Plant and Controller Open-Loop Gains

system is attenuated.

5.2.3.2 Track-Changing Maneuver

Figure 5-11 shows the dead-reckoned and actual trajectories of the ship during a track-changing maneuver. The actual nonlinear plant includes the effect of forward speed loss due to maneuvers. Thus, because the ship loses speed during the turn and experiences sway motion, it is not capable of completing the tight turn based solely upon kinematic relations. Further, the goal of the autopilot is only to maintain the desired heading rather than to regulate the cross-track error. A regulator of this type is described in the following section. The track error is approximately three ship lengths following the initial turn. This is reduced, however, during the second leg of the maneuver due to the sway velocity. The sway velocity in the second leg is opposite that of the initial leg. Thus, the ship actually moves back toward its dead-reckoned track on the second leg of the maneuver.

Figure 5-12 shows the actual and commanded heading angle during the track-changing maneuver. The errors in tracking the ramp input account for the cross-track errors in the trajectory. The tracking error in steady-state, however, is again less than 1%.

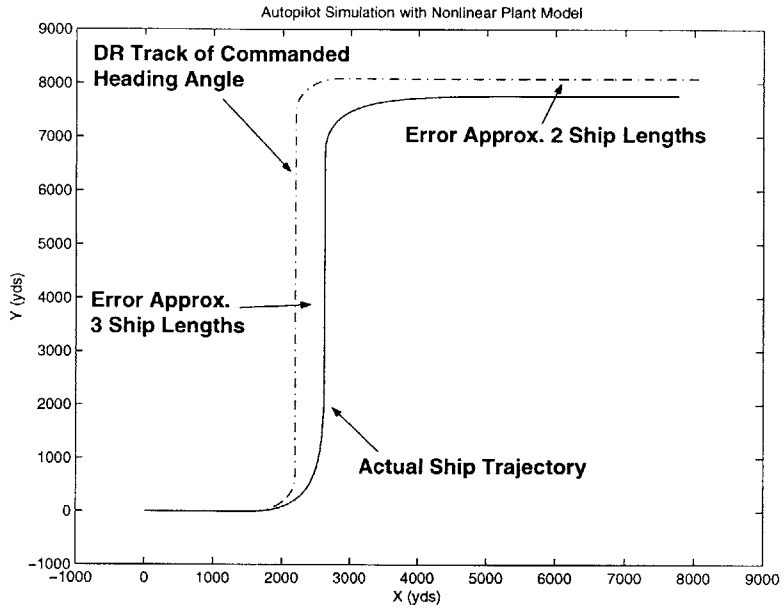

Figure 5-11: Nonlinear Plant Track-Changing Maneuver with Autopilot

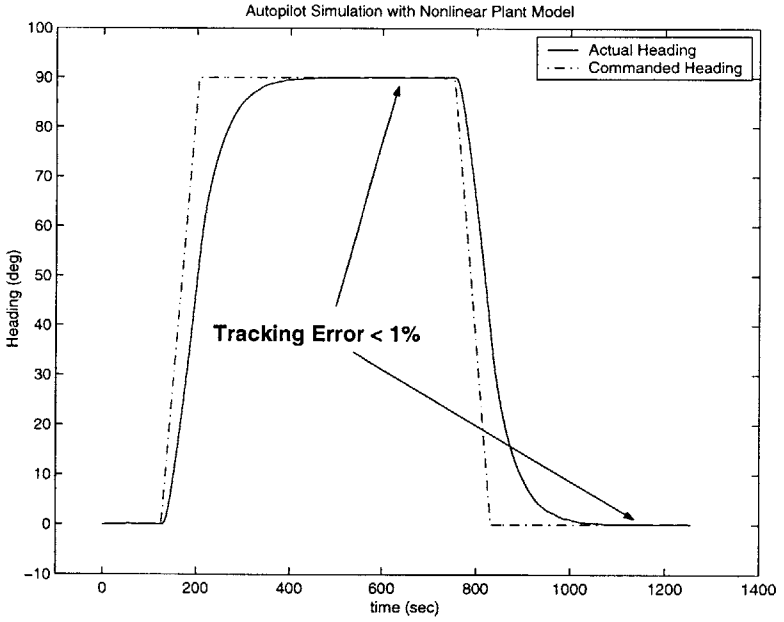

Figure 5-12: Nonlinear Plant Heading Angle during Track-Changing Maneuver with Autopilot

Figure 5-13 shows the commanded and actual rudder angles during the track-changing maneuver. Again, the rudder motion is quite smooth during the major portions of the maneuver and is not affected by the high-frequency controller commands. Further, notice that the rudder sweep during the maneuver is approximately 20^o over a period of about three minutes. Thus, the controller produces a slow, smooth rudder motion for the duration of the maneuver. The steady-state oscillations are again small and not deemed to cause excessive mechanical wear.

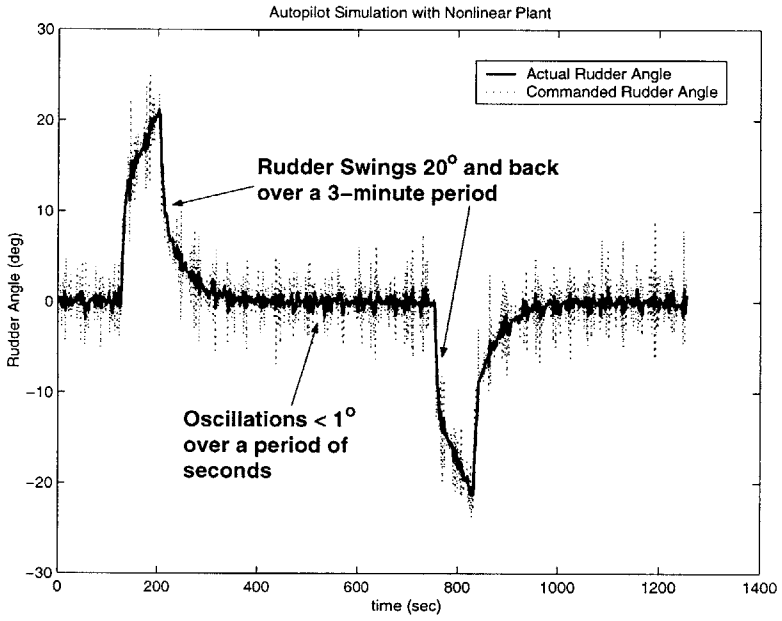

Figure 5-13: Actual and Commanded Rudder Angle During Track-Changing Maneuver

5.3 Cross-Track Error Controller Design

The goal of the cross-track error controller is to regulate the ship's lateral deviation from its intended track. The previous section demonstrated that an autopilot is not sufficient for this purpose. The controller must meet all criteria previously stated.

5.3.1 Dynamic Model

To begin the design of the cross-track error controller, the coordinate system was shifted. In the new coordinate system, the x-coordinate represents the distance traveled along the reference trajectory and the y-coordinate represents the lateral deviation from the intended track. The heading angle now represents the deviation from the desired heading angle along the intended track. The new coordinate system is illustrated in Figure 5-14. The kinematic

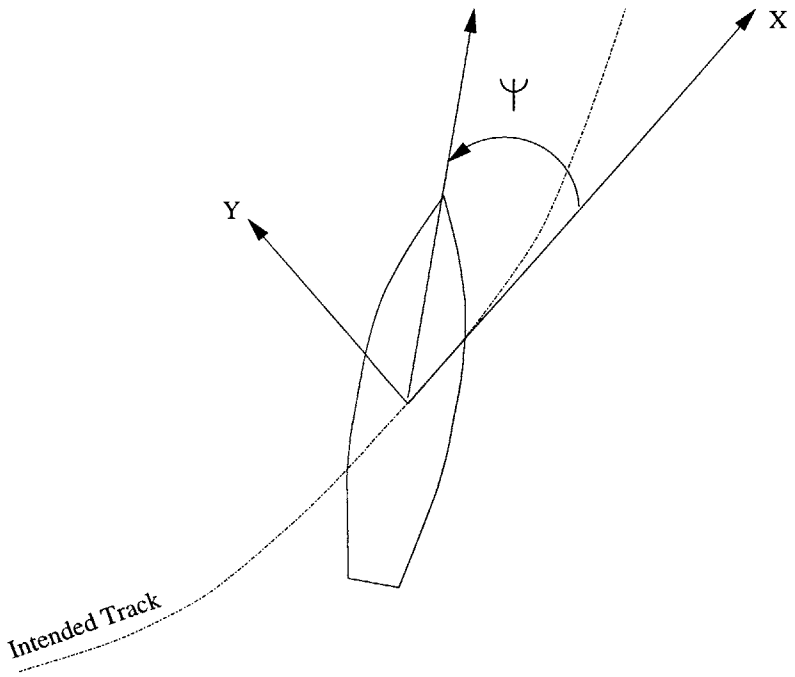

Figure 5-14: New Coordinate System for Track Controller

relations governing ship motions in this new coordinate system is given by the following equations:

$$\dot{x} = u\cos\psi - v\sin\psi \tag{5.35}$$

$$\dot{y} = u\sin\psi + v\cos\psi \tag{5.36}$$

Linearizing and non-dimensionalizing these equations leads to equation 5.37.

$$\dot{y} = \psi \tag{5.37}$$

where the dynamics of sway have again been removed as in 5.2.1. The dynamics of x have also been removed since it is not a control variable. Thus, differentiating equation 5.37 and inserting the result in equation 5.31 leads to the following expression for the control variable, y:

$$\ddot{y} = r \tag{5.38}$$

Thus, using SISO loopshaping control design theory, the track controller may be designed by simply adding an integrator to the plant transfer function given by equation 5.29. Thus, the new plant transfer function that maps the control input, δ_c, to the lateral track deviation, y, becomes:

$$P_y = \frac{P}{s} \tag{5.39}$$

5.3.2 Loopshaping Controller Design

Plants with double integrators can be problematic for the control systems engineer due to the phase shift introduced by the two poles at the origin. The two poles introduce a 180^o phase shift in the plant at DC. Thus, because the dynamics of yaw rate, r, behave as a second-order system, the phase decreases as frequency increases because the plant has slow poles.

The slope of the loopshape curve as it passes through the crossover frequency (where the magnitude is one) must satisfy the condition given by equation 5.40.

$$\frac{dL}{d\omega} \leq \frac{1}{\omega^2} \text{ around } \omega = \omega_c \tag{5.40}$$

The phase associated with this condition is -180^o. System stability requires that the phase be greater than this when the magnitude is one. Thus, the closed-loop system will be unstable if this condition is not met. Thus, the simple loopshaping design described in 5.2.2 may not be employed. In this instance, the controller must have some zeros to add the

required phase around the crossover frequency. Thus, the controller design must proceed by direct design of the controller, C [2], computation of S and T, and verification of the desired frequency response of the loop gain, $L = P_y C$. Thus, the general controller transfer function to start the design may be defined as follows:

$$C = \frac{k(s+z_1)(s+z_2)\dots(s+z_n)}{(s+p_1)(s+p_2)\dots(s+p_n)} \tag{5.41}$$

where n may be as many poles and zeros as required to achieve a desirable loopshape, subject to the requirement that the transfer function remain proper (degree of numerator $\leq$ degree of denominator) [11]. The final controller design may be described by the following transfer function:

$$C = \frac{20(s+0.5)^2(s+6)(s+1000)}{(s+11)(s+15)(s+30)^2} \tag{5.42}$$

Figure 5-15 illustrates the loopshape for the cross-track error controller design. The design proceeded iteratively by adding zeros and poles in the controller to achieve the desired frequency response properties. Figure 5-16 additionally shows the gain and phase

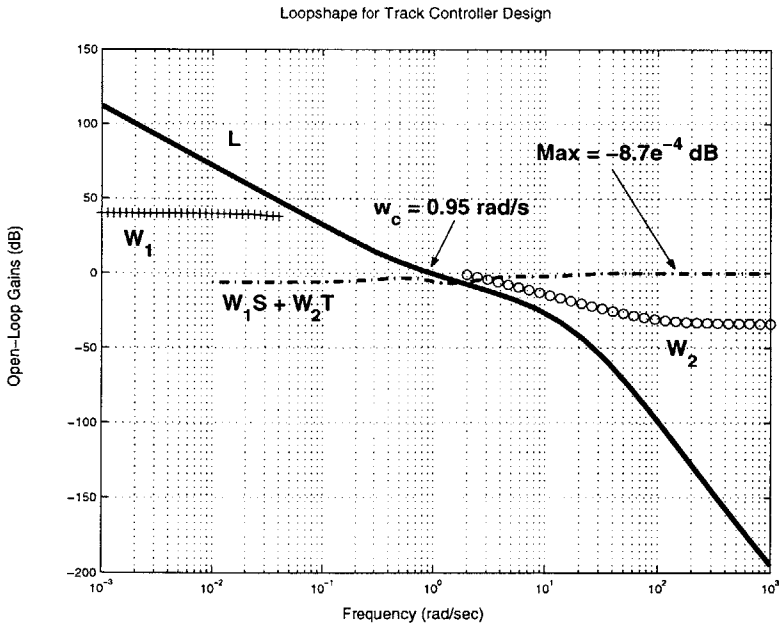

Figure 5-15: Loopshape for Cross-Track Error Controller Design

[2]Zeros and poles may be easily added and modified using the *zpk* function available in MATLAB.

margins associated with the design. Again, the margins fall well within the range of accepted practice. Notice in the phase plot of the Bode diagram how the controller adds phase to the system at frequencies below the crossover frequency, thus stabilizing the plant.

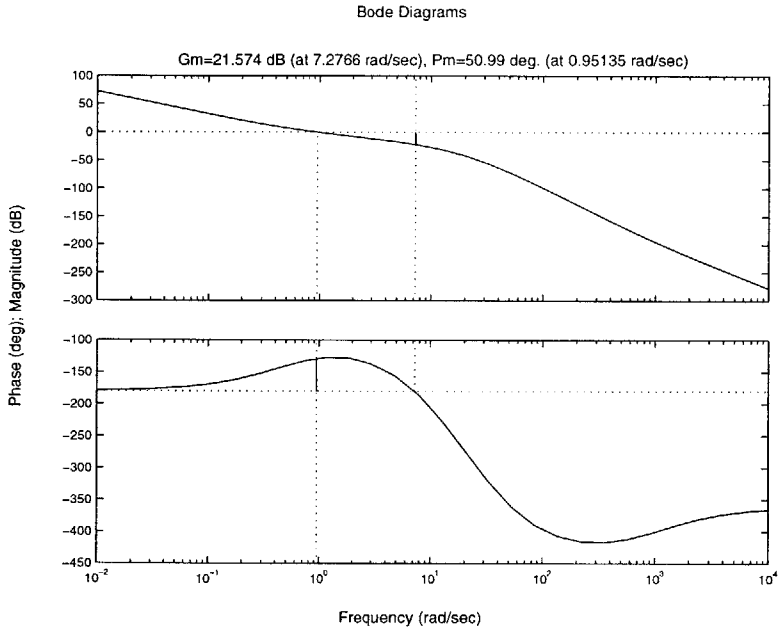

Figure 5-16: Gain and Phase Margins for Cross-Track Error Controller Design

Figure 5-17 illustrates the system closed-loop step response. The overshoot and settling time in this case may seem excessive when compared to conventional design practice. Compare, however, Figures 5-17 and 5-6, and consider equation 5.37. It would be extremely difficult, if not impossible, to command the dynamics of y to be faster than the dynamics of ψ because y depends solely upon ψ. Thus, its dynamics must be inherently slower. This physical fact is confirmed by the step response plot. Closed-loop simulation will subsequently show, however, that this controller performs extremely well on the nonlinear plant with smooth maneuvering trajectory commands.

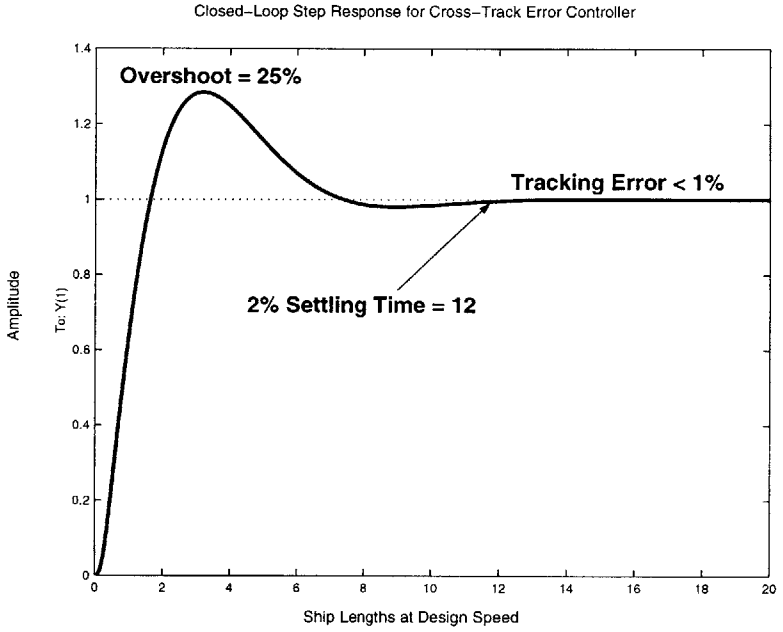

Figure 5-17: Cross-Track Error Controller Closed-Loop Step Response

5.3.3 Closed-Loop Simulation of the Cross-Track Error Controller

By shifting the coordinate system to the one shown in Figure 5-14, the two simulations performed in 5.2.3 may be combined into one simulation. The simulation speed is again 22 knots as in the previous simulations. The simulation steps are as follows:

1. The ship begins on a steady course and speed with no current.
2. After a short time, the ship experiences a current gust of 5 knots directly on its port beam.
3. Shortly thereafter, the ship makes a left turn, moves two ship lengths to port and steadies up.
4. After a period of steady travel, the ship executes a right turn and returns to its original track.

5.3.3.1 Maneuvering Simulation in Calm Seas with Current

Figure 5-18 shows the desired and actual trajectories as well as the heading angle during the maneuver. At the beginning of the maneuver, the controller takes strong action to reject

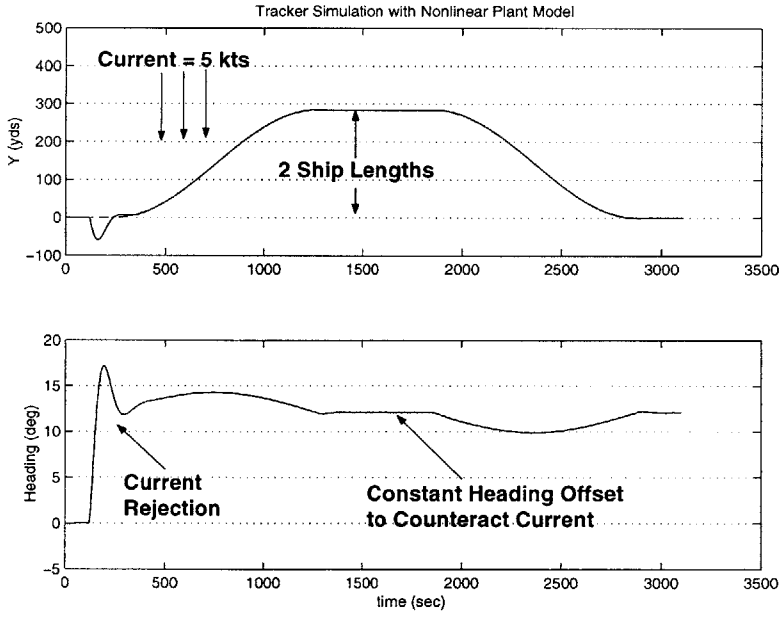

Figure 5-18: Trajectory and Heading during Nonlinear Plant Simulation

the current disturbance. It overshoots the desired track slightly upon its return and begins

to compensate. The left turn then executes and the ship follows the desired track with very small error until it steadies up. Notice that during the steady parts of the maneuver, the ship maintains a constant heading offset to counteract the current.

Figure 5-19 shows the commanded and actual rudder angle during the maneuver. The controller is again seen to respond significantly to the sensor noise for the same reason listed in 5.2.3.1. The most noteworthy item in this figure, however, is the way the controller senses

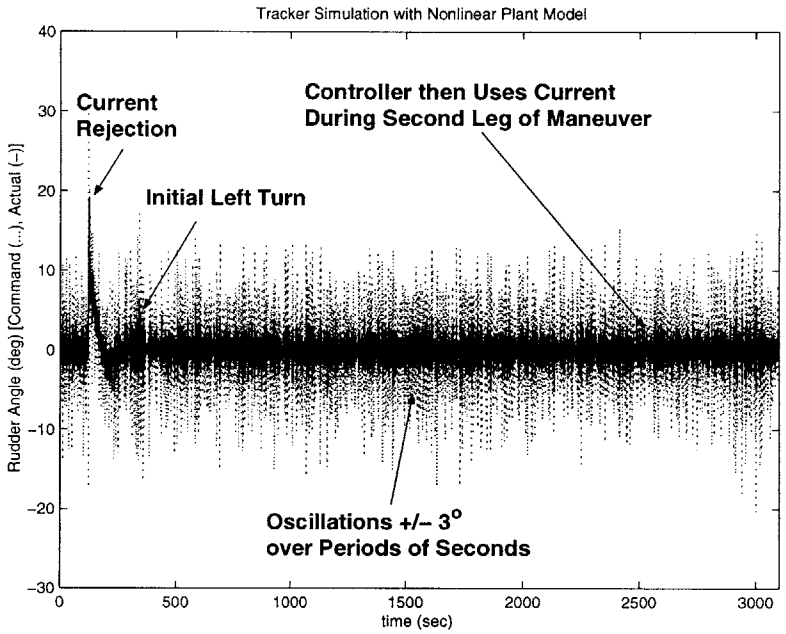

Figure 5-19: Actual and Commanded Rudder Angle During Nonlinear Plant Simulation

the current and uses it to execute the right turn to return to its original track. Note how the ship's heading decreases slightly below its offset, but does not pass through zero. Thus, the controller uses the current to allow the ship to be "blown" back onto its desired track.

Some may note that the ship requires a great deal of time (approximately 8 minutes) to complete the turning maneuvers. This may or may not be desirable. Smooth trajectories are required, however, to prevent the controller from over-compensating during the overshoot phase. This application could be extremely valuable, however, in maneuvers to avoid other vessels. For example, modern radar is capable of identifying contacts well before (longer than 8 minutes) their closest point of approach (CPA) time. Maneuvers to avoid other vessels are currently calculated by watchstanders using vector diagrams. Thus, a digital computer could calculate the CPA, compute a suitable track to avoid the contact by some

threshold distance, and then compute a smooth trajectory to maneuver to the new track, observe CPA, and maneuver back to the intended track.

5.3.3.2 Maneuver in Sea State 4 with 5-Knot Current

The simulation would not be complete without verifying the controller's performance in a sea state. The sea state is modeled as a random disturbance and filtered to preserve only the low-frequency components. Table 6 of [38] indicates that a state four sea has a significant wave height of 1.25-2.5 meters (4 - 8 feet). Additionally, Table 3 of [38] indicates that waves of this height represent sea conditions with the highest probability of occurrence worldwide. Thus, sea state four was chosen for simulation. Figure 5-20 shows the wave spectrum and Figure 5-21 shows the time history of the wave heights.

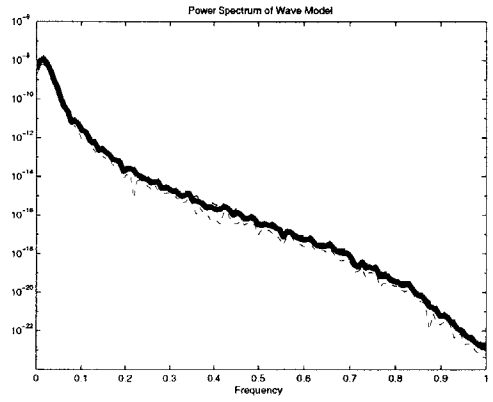

Figure 5-20: Power Spectrum of Wave Model

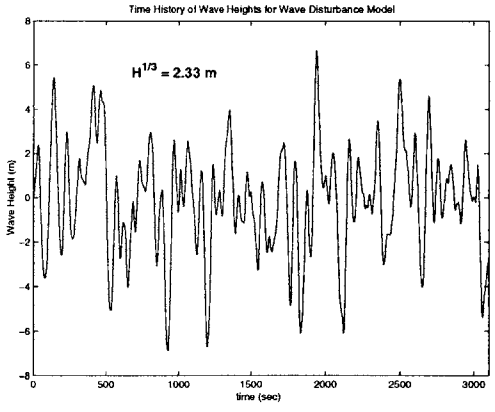

Figure 5-21: Time History of Wave Heights

The same maneuver described in 5.3.3 is performed with the current and sea state introduced as disturbances. Figure 5-22 shows the actual and commanded trajectories as well as the heading angle during the maneuver. Notice that, similar to the maneuver in calm seas, the controller maintains a constant heading offset to counteract the effects of the current. The low-frequency wave disturbances, however, cause the ship to deviate from its commanded track. Thus, the ship oscillates a small amount about its commanded track. The amplitude of the oscillations, however, is less than 20 yards (about 15% of the ship length).

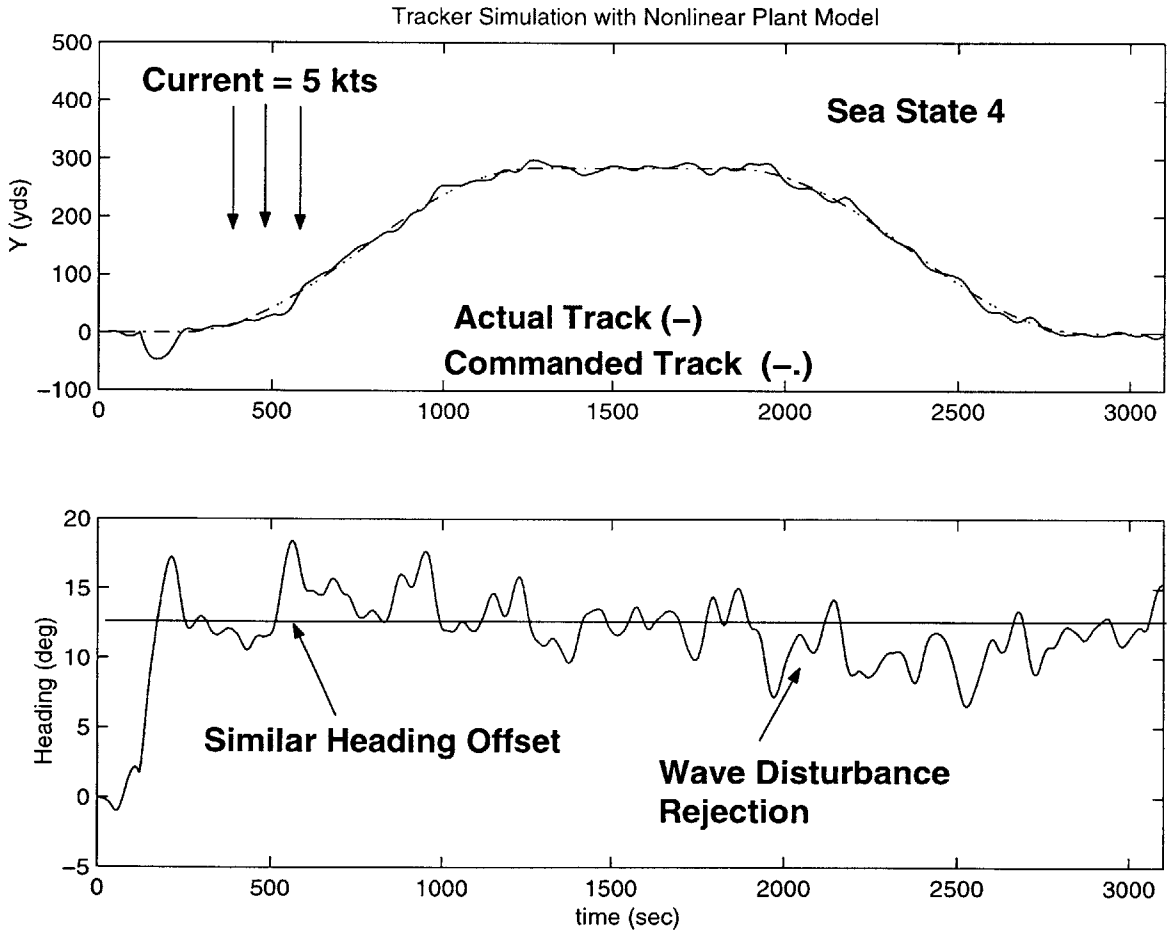

Figure 5-22: Trajectory and Heading During Track Change

Figure 5-23 shows the commanded and actual rudder angles during the maneuver. Careful examination of Figure 5-23 indicates a low-frequency signal among the high-frequency measurements driving the controller. It is this low-frequency command signal that allows the ship to remain on track despite the disturbances.

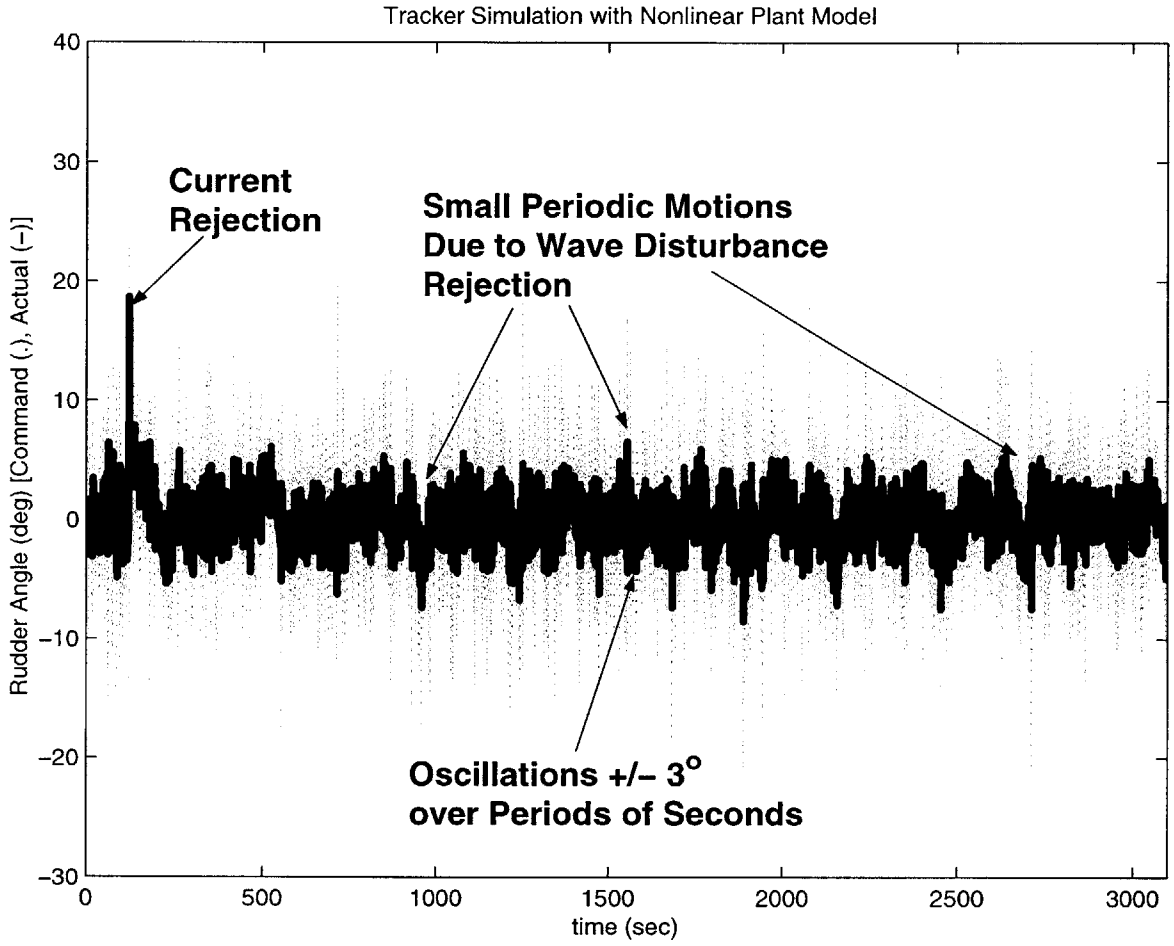

Figure 5-23: Commanded and Actual Rudder Angle during Track Change

This low-frequency component may be seen more clearly in Figure 5-24. This figure shows the time history during the steady portion of the maneuver between the two turns. Notice how the rudder corrective actions exhibit a period similar to that of the ship deviations about its intended track. In particular, the figure shows the rudder's large corrective action applied at the point about 1400 seconds into the simulation. This is the point where the ship exhibits its largest track deviation due to overshoot at the end of the turn. The controller senses this, however, and takes the appropriate action.

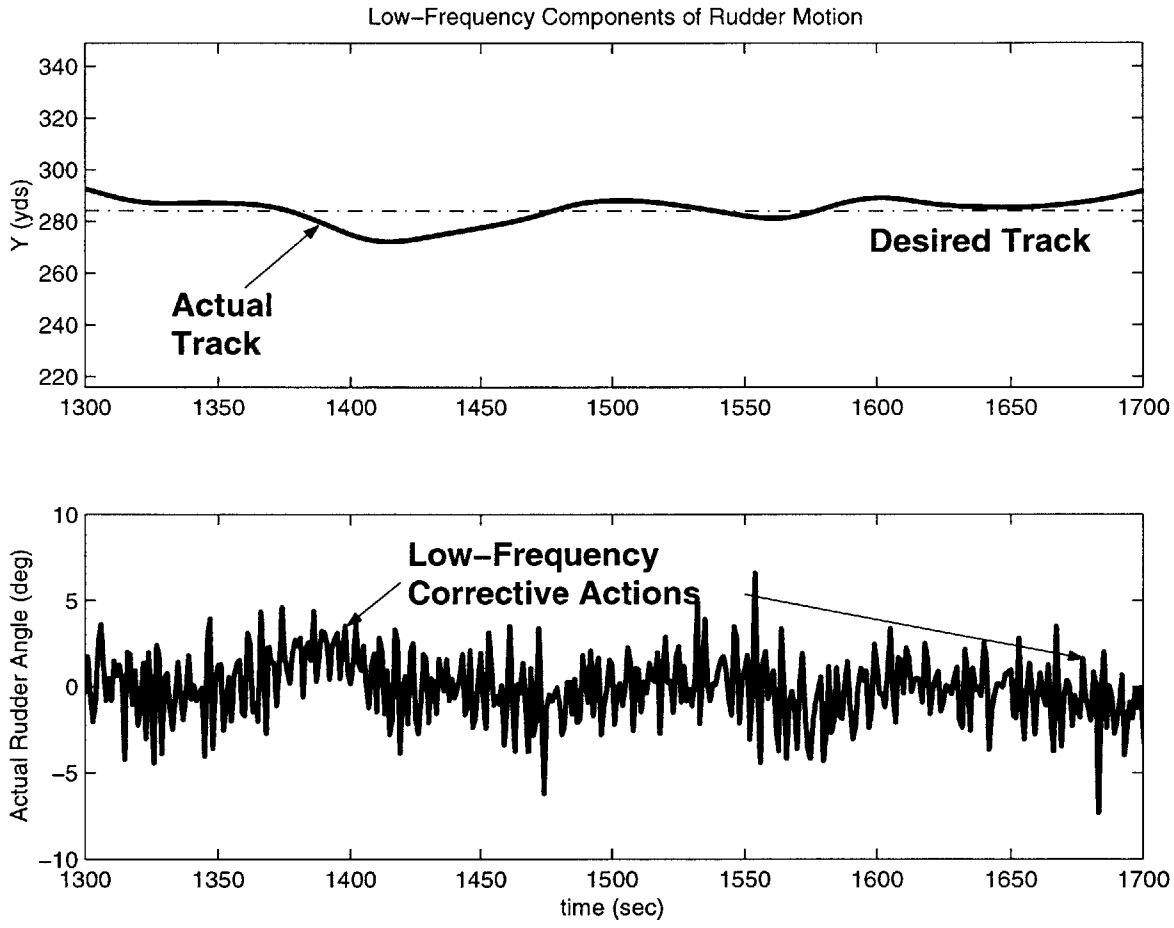

Figure 5-24: Low-Frequency Component of Actual Rudder Angles

Chapter 6

Conclusion

6.1 Summary

This work gives rise to a systematic method for adding automatic maneuvering control system design to the macroscopic ship design process. The procedure may be summarized as follows:

1. Build a scale model of the ship.
2. Outfit the model with sensors.
3. Conduct a series of controlled maneuvers with the model to gather data.
4. Design a SAEKF and use the data collected from the model to identify the ship hydrodynamic coefficients.
5. Use the identified coefficients to develop controllers.
6. Test the controller designs on the scale model.

This work accomplishes a piece of this process by identifying the linear damping derivatives and developing control laws based upon them. Specifically, this work accomplished the following objectives:

- Selection of an assumed form of the equations of ship motion in the horizontal plane.
- Design of a SAEKF to identify the linear damping hydrodynamic coefficients within these equations.
- Successful identification of these coefficients which are the most critical to overall ship

maneuvering stability in the horizontal plane.

• Design of two simple controllers that may be tested on scale ship models to determine their performance.

The current method of identifying these terms involves large towing tanks and rotating arm basins. It also requires extensive labor to operate the equipment. These requirements are in addition to the need for a scale model of the ship. Thus, development of the ideas introduced in [3] and [43] and continued here may not only lead to an efficient, effective process for adding maneuvering automation to the ship design process, it may also reduce the infrastructure required to support it.

6.2 Conclusions

The following list summarizes the items deemed most noteworthy by the author over the course of this study.

1. The EKF method shows definite feasibility as a method to determine linear ship hydrodynamic coefficients. These parameters may then form the basis for simple controller designs that can be tested on scale models.

2. The parameter estimates provided by the SAEKF need not be very accurate to provide values suitable for controller design. The parameters determined in this study reproduced simulation trajectories with approximately 15% error in steady turning diameter. Errors as large as 40%, however, may very likely yield acceptable controller designs for slow maneuvers.

3. The dynamics of sway need not be considered to develop effective linear controllers for the types of maneuvers considered in this study. Thus, controller designs for these types of maneuvers may be based on only two parameters.

4. The EKF performs extremely well as a *state estimator* (due to the physical state measurements) despite significant inaccuracies in the filter dynamic model. Specifically, the SAEKF model used in this study was completely linear, but still produced very accurate estimates of the physical states (u, v, r, and n) of the nonlinear plant model used to generate the measurement data. The dynamics of u and n, in fact, were completely ignored in propagating the filter state estimates.

5. The performance of the SAEKF as a *parameter estimator*, however, will degrade if the filter model is not sufficiently accurate in describing the actual plant. The modeling errors will cause significant bias in the parameter estimates.

6. The instantaneous rudder angle of attack decreases rapidly with respect to the nominal angle of attack as sway speed and yaw rate increase. Thus, the linear lift coefficient assumption proved to be valid in the maneuvers conducted in this study despite the use of rudder angles traditionally believed to lie outside the linear regime.

6.3 Recommendations for Further Study

As in any other design study, this work leaves several areas that require further thought and development. Among these, the most important in the author's mind may be summarized as follows:

1. This work considers performing the identification in calm water. Environmental disturbances such as wind and waves could have a significant effect on the identification process. The magnitude of these effects should be investigated.

2. Rolling motions have an effect on maneuvering in the horizontal plane. Thus, the inclusion of rolling motions in the nonlinear model could have an effect on the linear controller performance. The magnitude of these effects should be investigated.

3. Despite the identification of four terms in this study, these four terms were reduced to two to develop the controllers. Identification of only these two terms using an SAEKF may be possible. This could make the implementation of the SAEKF much simpler.

4. The EKF provided very accurate estimates of the surge speed and propeller rotational speed despite the fact that its model completely ignored their dynamics. These quantities are easily measured by the speed log and a shaft tachometer. Thus, perhaps the EKF could be used to provide state estimates for a MIMO controller to control the ship's x-coordinate as well as its y-coordinate.

5. The proper noise covariance terms are an important design parameter in any Kalman filter implementation. This study determined the correct noise covariances through an iterative procedure of identification and simulation. Inclusion of the noise covariances

as filter parameters to be estimated may reduce the iterative nature of this process and lead to a more efficient design process.

6. Implement the method outlined herein on the DDG-51 scale model developed at the MIT Towing Tank.

7. Investigate the range over which the assumption of linearized lift on rudders is valid by accounting for the ship dynamics in computing the instantaneous angle of attack.

Appendix A

State Augmentation of the Extended Kalman Filter

The derivations presented in section 2.2 hold for estimation of the state vector describing a nonlinear system. Augmentation of the state vector for use in estimating unknown parameters is the subject of the sequel.

Recall equations 2.10 and 2.19 in 2.2.2 and 2.2.3, respectively. The variable $\underline{\hat{x}}$ represents the estimate of the states describing the physical system. Therefore, the estimated state vector can be augmented with the unknown parameters in the system to allow them to be estimated along with the system states. In the case of DDG-51, the unkown parameters are constant hydrodynamic maneuvering coefficients. Maneuvering coefficients may change with changes in submerged geometry, speed, etc. Nondimensionalization of the equations removes speed considerations and submerged geometry certainly changes slowly with time. DDG-51's compensated fuel system, however, ensures that the ship maintains nearly constant draft over its entire range of operation. Therefore, the state vector is augmented with the unknown system parameters whose derivatives are zero. For example, to estimate an unknown parameter, b, in a system fully described by states x_1 and x_2, the state vector and

associated **F** matrix would be augmented as follows:

$$\begin{bmatrix} \dot{x_1} \\ \dot{x_2} \\ \dot{b} \end{bmatrix} = \begin{bmatrix} f_1(x_1, x_2, \beta, t) \\ f_2(x_1, x_2, \beta, t) \\ 0 \end{bmatrix} \tag{A.1}$$

$$\mathbf{F} = \begin{bmatrix} \frac{\partial f_1}{\partial x_1} & \frac{\partial f_1}{\partial x_2} & \frac{\partial f_1}{\partial \beta} \\ \frac{\partial f_2}{\partial x_1} & \frac{\partial f_2}{\partial x_2} & \frac{\partial f_2}{\partial \beta} \\ 0 & 0 & 0 \end{bmatrix} \tag{A.2}$$

Using this methodology, an initial estimate is made for the unknown parameters in the augmented state vector and the associated error in the estimate. The parameters are then estimated in exactly the same manner as the state vector. Once the state vector has been augmented with the unknown parameters, and the **F** matrix modified appropriately, the EKF becomes the SAEKF. The following section presents an example application of the SAEKF.

A.1 Application of the State Augmented Extended Kalman Filter to a Nonlinear Tracking Problem

The Extended Kalman Filter has proven to be extremely effective for tracking applications (such as tracking an object with a radar). The radar provides position information for the object, but no velocity information. Effective tracking, however, requires velocity information to fully describe the state of the system.

Assume for simplicity that an object falls through space directly toward a tracking radar as illustrated in Figure A-1 (i.e. a one-dimensional tracking problem)[1]. Assume further that the system has an unknown parameter (the ballistic coefficient, b) which affects the drag force on the object as it falls through space. The goal is to estimate the velocity of the object, v, and the unknown parameter, b, with only noisy measurements of its position, x, available as actual data. The nonlinearity arises through the dependence of drag on the square of the object's velocity and the ballistic coefficient ($d(b) \propto v^2$).

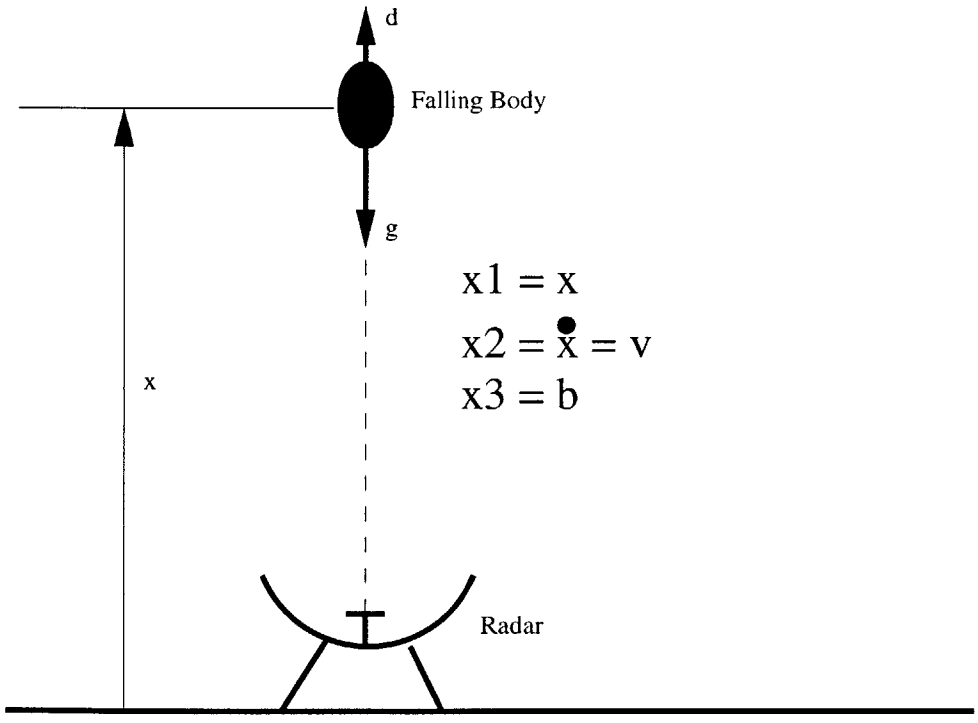

Figure A-1: A One-Dimensional Nonlinear Tracking Problem

[1]This example is taken from example 6.1-2 in [19].

Figure A-2 illustrates the results. The upper plot shows the filter's ability to very accurately estimate the object's velocity as it falls through the atmosphere. The lower plot illustrates the filter's ability to converge on the true value of the ballistic coefficient using the measurements and computed gains. The filter does not change much initially because the object experiences very little drag high in the atmosphere. As the object enters the dense atmosphere the filter converges to the true value and remains there. Thus, one concludes that the filter has difficulty identifying the parameter value if it does not significantly affect the dynamics.

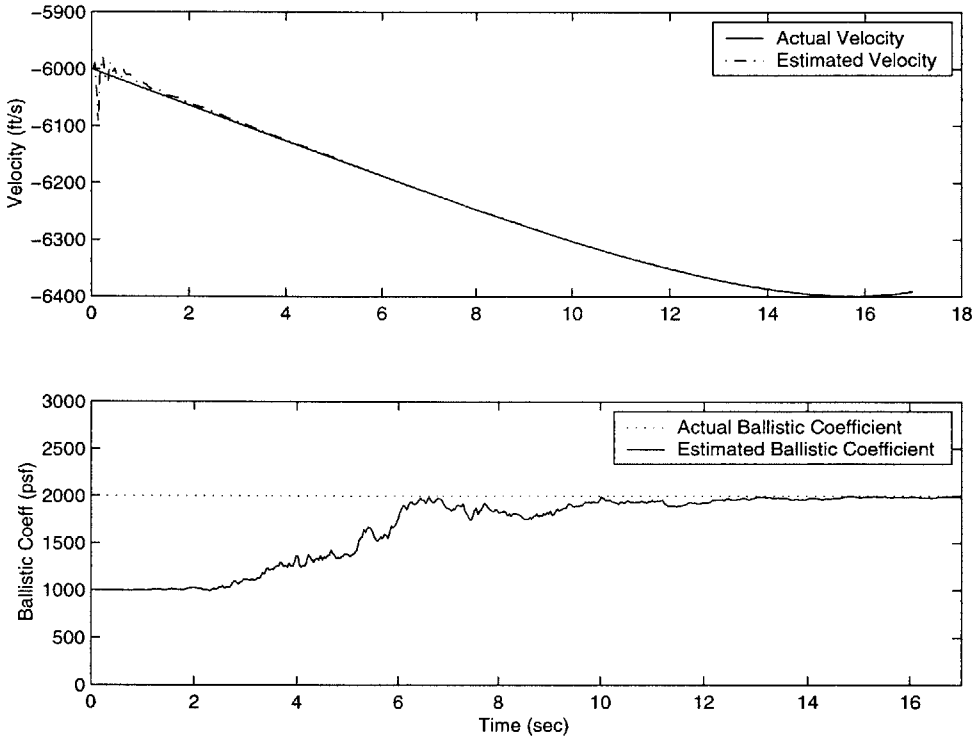

Figure A-2: EKF Application

References

[1] PDI Report 336091-01. Design and Analysis of an Alternative Programmed Control Module (PCM) for DDG-51 Class Ships". Technical report, Propulsion Dynamics, Inc., February 1994.

[2] M. A. Abkowitz. *Lectures in Ship Hydrodynamics, Steering, and Maneuverability.* MIT Press, Cambridge, MA, 1964.

[3] M. A. Abkowitz. Measurement of Hydrodynamic Characteristics from Ship Maneuvering Trials by System Identification. *SNAME Transactions*, 88:283–318, November 1980.

[4] B. D. O. Anderson and J. B. Moore. *Optimal Filtering.* Prentice-Hall, Inc., Englewood Cliffs, NJ, 1987.

[5] M. Blanke. *Ship Propulsion Losses Related to Automated Steering and Prime Mover Control.* PhD thesis, The Technical University of Denmark, Lyngby, Denmark, 1981.

[6] H. L. Brinati. System Identification Applied to Maneuvering Trials. Master's thesis, Massachusetts Institute of Technology, Department of Ocean Engineering, 1973.

[7] J. Chudley et al. A review of mathematical model used in ship manoevers. In *Proceedings of Computer Methods in Marine and Offshore Engineering*, Florida, USA, 1991.

[8] D. L. Coble. A Flight Test Sutdy to Determine Aircraft Propulsive Efficiency and Aerodynamic Drag Using an Extended Kalman Filter Parameter Identification Technique and Lock's Propeller Model. Master's thesis, Mississippi State University, Department of Aerospace Engineering, 1992.

[9] E. Z. Crues. Use of the Modified Gain Extended Kalman Filter in the Identification of Aircraft Stability Derivatives. Master's thesis, The University of Texas at Austin, Austin, Texas, 1985.

[10] I. W. Dand et al. Report of the manoeuverability committee. In *Proceedings of the 20th International Towing Tank Conference*, pages 309–361, Seoul, Korea, 1993.

[11] J. C. Doyle et al. *Feedback Control Theory.* Macmillan Publishing Company, New York, NY, 1992.

[12] R. J. Fitzgerald. Divergence of the Kalman Filter. *IEEE Transactions on Automatic Control*, AC-16:736–747, December 1971.

[13] T. I. Fossen. *Guidance and Control of Ocean Vehicles.* John Wiley & Sons, New York, NY, 1994.

[14] B. Friedland. Treatment of Bias in Recursive Filtering. *IEEE Transactions on Automatic Control*, AC-14:359–367, August 1969.

[15] B. Friedland. *Control System Design: An Introduction to State-Space Methods.* McGraw-Hill, Inc., New York, NY, 1986.

[16] W. P. Fun. An Explicit Adaptive Flight Control System Based on the Modified Gain Extended Kalman Filter. Master's thesis, The University of Texas at Austin, Austin, Texas, 1986.

[17] J. B. Garcia-Velo. Parameter Estimation of an Unstable Aircraft Using an Extended Kalman Filter. Master's thesis, University of Cincinnati, Department of Aerospace Engineering and Engineering Mechanics, 1991.

[18] J. B. Garcia-Velo. *Determination of Noise Covariances for Extended Kalman Filter Parameter Estimators to Account for Modeling Errors.* PhD thesis, University of Cincinnati, Department of Aerospace Engineering and Engineering Mechanics, 1997.

[19] A. Gelb et al. *Applied Optimal Estimation.* MIT Press, Cambridge, MA, 1974.

[20] D. B. Grunberg. *Guaranteed Properties of the Extended Kalman Filter.* Massachusetts Institute of Technology, Cambridge, MA, 1987.

[21] M. N. Hayes. *Parametric Identification of Nonlinear Stochasitc Systems Applied to Ocean Vehicle Dynamics.* PhD thesis, Massachusetts Institute of Technology, Department of Ocean Engineering, 1971.

[22] H. Heffes. The Effect of Erroneous Models on the Kalman Filter Response. *IEEE Transactions on Automatic Control*, AC-11:541–543, July 1966.

[23] T. Holtzhüter. A workable dynamic model for the track control of ships. In *Proceedings of the 9^{th} Ship Control Systems Symposium*, pages 4.275–4.298, Maryland, USA, 1990.

[24] W. Y. Hwang. *Application of System Identification to Ship Maneuvering.* PhD thesis, Massachusetts Institute of Technology, Department of Ocean Engineering, 1980.

[25] S. Inoue et al. Hydrodynamic derivatives in ship maneuvering. *International Shipbuilding Progress*, 28:112–125, No. 321 1981.

[26] S. Inoue et al. A practical calculation method of ship maneuvering motion. *International Shipbuilding Progress*, 28:207–222, No. 325 1981.

[27] R. Isermann et al. *Adaptive Control Systems.* Prentice Hall, New York, NY, 1992.

[28] C. G. Kallstrom et al. A track autopilot predictor system for ships. In *Proceedings of the 11^{th} Ship Control Systems Symposium*, Southamptom, UK, 1997.

[29] R. E. Kalman. A New Approach to Linear Filtering and Prediction Problems. *Transactions of the American Society of Mechanical Engineers, Journal of Basic Engineering*, 82:34–35, March 1960.

[30] R. E. Kalman and R. S. Bucy. New Results in Linear Filtering and Prediction Theory. *Transactions of the American Society of Mechanical Engineers, Journal of Basic Engineering*, 83:95–107, December 1961.

[31] J. E. Kerwin. *Class Notes for Propellers and Hydrofoils.* Massachusetts Institute of Technology, Cambridge, MA, 1996.

[32] O. Kohei et al. A Robust Autopilot System Against the Various Sea Conditions: Noise Adaptive Autopilot. *Ship Operation Automation*, 7, March 1979.

[33] F. L. Lewis. *Applied Optimal Control and Estimation.* Prentice Hall, Englewood Cliffs, NJ, 1992.

[34] L. Ljung. *System Identification: Theory for the User.* Prentice-Hall, Inc., Englewood Cliffs, NJ, 1987.

[35] J. G. Lundblad. Application of the Extended Kalman Filtering Technique to Ship Maneuvering Analysis. Master's thesis, Massachusetts Institute of Technology, Department of Ocean Engineering, 1975.

[36] Driels M. *Linear Control Systems Engineering.* McGraw-Hill, Inc., New York, NY, 1996.

[37] P. Mandel et al. *Principles of Naval Architecture.* SNAME, Chapter 9, Section 2, 1988.

[38] P. Mandel et al. *Principles of Naval Architecture.* SNAME, Chapter 8, Section 2, 1988.

[39] R. K. Mehra. On The Identification of Variances and Adaptive Kalman Filtering. *IEEE Transactions on Automatic Control*, AC-15:175–184, April 1970.

[40] T. Nishimura. On the A Priori Information in Sequential Estimation Problems. *IEEE Transactions on Automatic Control*, AC-11:197–204, April 1966.

[41] N. H. Norrbin et al. *The Identification of Linear Ship Steering Dynamics Using Maximum Likelihood Parameter Estimation.* Swedish State Shipbuilding Experimental Tank, Göteborg, Sweden, 1975.

[42] C. L. Phillips and R. D. Harbor. *Feedback Control Systems.* Prentice-Hall, Inc., Upper Saddle River, NJ, 2000.

[43] R. E. Quezada Ojeda. Robust Control Design and Simulation of the Maneuvering Dynamics of an Arleigh Burke Class Destroyer. Master's thesis, Massachusetts Institute of Technology, Department of Ocean Engineering, 1999.

[44] F. H. Schlee et al. Divergence in the Kalman Filter. *AIAA Journal*, 5:1114–1120, June 1967.

[45] M. M. Sidar and B. F. Doolin. On The Feasbility of Real-Time Prediction of Aircraft Carrier Motion at Sea. *IEEE Transactions on Automatic Control*, AC-28:350–355, March 1983.

[46] T. T. Soong. On A Priori Statistics in Minimum-Variance Estimation Problems. *Transactions of the American Society of Mechanical Engineers, Journal of Basic Engineering*, 87:109–112, March 1965.

[47] F. F. Szeto. System Identification Techniques for Ship Maneuvering Trials. Master's thesis, Massachusetts Institute of Technology, Department of Ocean Engineering, 1977.

[48] L. S. Taek. *A Stochastic Analysis of a Modified Gain Extended Kalman Filter.* PhD thesis, The University of Texas at Austin, Austin, Texas, 1984.

[49] M. S. Triantafyllou. *Class Notes for Maneuvering and Control of Surface and Underwater Vehicles.* Massachusetts Institute of Technology, Cambridge, MA, 1996.

[50] J. Van de Vegte. *Feedback Control Systems.* Prentice Hall, Englewood Cliffs, NJ, 1994.

[51] J. Wunnenberg. Convergence of the Extended Kalman Filter. Master's thesis, University of Washington, Seattle, Washington, 1985.

[52] Y. Yansheng. Study of ship maneuvering mathematical model in shiphandling simulator. In *Proceedings of MARSIM and ICSM*, pages 607–615, Copenhagen, Denmark, 1996.

[53] K. Zhou and J. C. Doyle. *Essentials of Robust Control.* Prentice Hall, Upper Saddle River, NJ, 1998.

[54] W. Zhou. *Identification of Nonlinear Marine Systems.* Servolaboratory, Technical University of Denmark, Lyngby, Denmark, 1987.